The HOSTS Survey for Exozodiacal Dust: Observational Results from the Complete Survey

S. Ertel[1,2], D. Defrère[3], P. Hinz[2], B. Mennesson[4], G. M. Kennedy[5], W. C. Danchi[6], C. Gelino[4], J. M. Hill[1], W. F. Hoffmann[2], J. Mazoyer[4], G. Rieke[2], A. Shannon[7,8,9], K. Stapelfeldt[4], E. Spalding[2], J. M. Stone[2,17], A. Vaz[2], A. J. Weinberger[10], P. Willems[4], O. Absil[3,18], P. Arbo[2], V. P. Bailey[4], C. Beichman[11], G. Bryden[4], E. C. Downey[2], O. Durney[2], S. Esposito[12], A. Gaspar[2], P. Grenz[2], C. A. Haniff[13], J. M. Leisenring[2], L. Marion[3], T. J. McMahon[2], R. Millan-Gabet[11], M. Montoya[2], K. M. Morzinski[2], S. Perera[2,14], E. Pinna[12], J.-U. Pott[14], J. Power[1], A. Puglisi[12], A. Roberge[6], E. Serabyn[4], A. J. Skemer[15], K. Y. L. Su[2], V. Vaitheeswaran[2], and M. C. Wyatt[16]

[1] Large Binocular Telescope Observatory, 933 North Cherry Avenue, Tucson, AZ 85721, USA; sertel@email.arizona.edu
[2] Steward Observatory, Department of Astronomy, University of Arizona, 993 N. Cherry Avenue, Tucson, AZ, 85721, USA
[3] Space sciences, Technologies & Astrophysics Research (STAR) Institute, University of Liège, Liège, Belgium
[4] Jet Propulsion Laboratory, California Institute of Technology, 4800 Oak Grove Drive, Pasadena, CA 91109, USA
[5] Department of Physics, University of Warwick, Gibbet Hill Road, Coventry CV4 7AL, UK
[6] NASA Goddard Space Flight Center, Exoplanets & Stellar Astrophysics Laboratory, Code 667, Greenbelt, MD 20771, USA
[7] LESIA, Observatoire de Paris, PSL Research University, CNRS, Sorbonne Université, Université Paris Diderot, Sorbonne Paris Cité, 5 Place Jules Janssen, F-92195 Meudon, France
[8] Department of Astronomy and Astrophysics, The Pennsylvania State University, State College, PA 16801, USA
[9] Center for Exoplanets and Habitable Worlds, The Pennsylvania State University, State College, PA 16802, USA
[10] Department of Terrestrial Magnetism, Carnegie Institution of Washington, 5241 Broad Branch Road NW, Washington, DC 20015, USA
[11] NASA Exoplanet Science Institute, MS 100-22, California Institute of Technology, Pasadena, CA 91125, USA
[12] INAF-Osservatorio Astrofisico di Arcetri, Largo E. Fermi 5, I-50125 Firenze, Italy
[13] Cavendish Laboratory, University of Cambridge, JJ Thomson Avenue, Cambridge CB3 0HE, UK
[14] Max Planck Institut für Astronomie, Königstuhl 17, D-69117 Heidelberg, Germany
[15] Astronomy Department, University of California Santa Cruz, 1156 High Street, Santa Cruz, CA 95064, USA
[16] Institute of Astronomy, University of Cambridge, Madingley Road, Cambridge CB3 0HA, UK

Abstract

The Large Binocular Telescope Interferometer (LBTI) enables nulling interferometric observations across the N band (8 to 13 μm) to suppress a star's bright light and probe for faint circumstellar emission. We present and statistically analyze the results from the LBTI/Hunt for Observable Signatures of Terrestrial Systems survey for exozodiacal dust. By comparing our measurements to model predictions based on the solar zodiacal dust in the N band, we estimate a 1σ median sensitivity of 23 zodis times the solar system dust surface density in its habitable zone (HZ; 23 zodis) for early-type stars and 48 zodis for Sun-like stars, where 1 zodi is the surface density of HZ dust in the solar system. Of the 38 stars observed, 10 show significant excess. A clear correlation of our detections with the presence of cold dust in the systems was found, but none with the stellar spectral type or age. The majority of Sun-like stars have relatively low HZ dust levels (best-fit median: 3 zodis, 1σ upper limit: 9 zodis, 95% confidence: 27 zodis based on our N band measurements), while ~20% are significantly more dusty. The solar system's HZ dust content is consistent with being typical. Our median HZ dust level would not be a major limitation to the direct imaging search for Earth-like exoplanets, but more precise constraints are still required, in particular to evaluate the impact of exozodiacal dust for the spectroscopic characterization of imaged exo-Earth candidates.

Unified Astronomy Thesaurus concepts: Exozodiacal dust (500); Debris disks (363); Habitable zone (696); Habitable planets (695)

1. Introduction

Imaging habitable exoplanets (exo-Earth imaging) is one of the major challenges of modern astronomy. The main technical challenges are the required high contrast and small inner working angle resulting from the faintness of the planets and their proximity to the bright host stars. In addition, exozodiacal dust constitutes an astrophysical challenge for exo-Earth imaging to be understood and potentially to be overcome (Roberge et al. 2012). This analog to the zodiacal dust in our solar system (Kelsall et al. 1998; Dermott et al. 2002; Nesvorný et al. 2010) is expected to be present in and near the habitable zones (HZs) of the exo-Earth imaging mission target stars. The presence of large amounts of exozodiacal dust in a system represents a major source of photon noise that may render a faint planet undetectable. Furthermore, spatial structures in the dust distribution may add confusion and be misinterpreted as planets due to the limited angular resolution and signal-to-noise ratio (S/N) of the observations (Defrère et al. 2012b). Smaller amounts of smoothly distributed dust may still make an imaged planet's spectroscopic characterization prohibitively time consuming. As a consequence, the occurrence rate and typical brightness of massive exozodiacal dust systems affect the yield of future exo-Earth imaging missions and are thus important factors for the mission design (aperture size, mission duration, target selection; Defrère et al. 2010; Stark et al. 2015, 2016, 2019).

---

[17] Hubble fellow.
[18] F.R.S.-FNRS Research Associate.

In addition, studying the dust distribution provides present-day insight into the characteristics of HZs around nearby stars (Kral et al. 2017). Dust in and near the HZ of a star (HZ dust) has a temperature around 300 K and is best detected near the peak of its spectral energy distribution near 10 μm. This dust is distinct from colder dust in a debris disk farther out in the system that is typically detected photometrically in the far-infrared (exo-Kuiper belts) and can most often be explained by continuous dust production in an equilibrium collisional cascade (Dohnanyi 1969; Backman & Paresce 1993). Inside these outer belts, many systems have dust at temperatures similar to those in the asteroidal zone of the solar system (Morales et al. 2011; Kennedy & Wyatt 2014), which may similarly originate from a local equilibrium collisional cascade or have an origin similar or related to that of the HZ dust discussed below (including belt formation due to planet–disk interaction; e.g., Ertel et al. 2012b; Shannon et al. 2015). The HZ dust is also different from the hot excesses detected around nearby stars using optical long-baseline interferometry and usually attributed to dust emission even closer in (Absil et al. 2006, 2013; Ertel et al. 2014a), while the mechanisms producing this hot dust may or may not be related to those producing the HZ dust (Kennedy & Piette 2015; Rieke et al. 2016; Faramaz et al. 2017; Kimura et al. 2020; Sezestre et al. 2019).

The HZ dust may be produced through collisions of planetesimals in an outer, Kuiper, or asteroid-belt-like debris disk and migrate inward due to Poynting–Robertson (PR) drag and stellar wind drag (Wyatt 2005; Reidemeister et al. 2011). The amount of dust that reaches the HZ may then be used to constrain the presence of planets between the outer reservoir and the HZ that prevent a fraction of the dust from migrating (Moro-Martín & Malhotra 2003; Bonsor et al. 2018). Alternatively, the dust may be produced by comets sublimating or otherwise disintegrating when they reach the HZ from farther out in the system (Nesvorný et al. 2010; Faramaz et al. 2017; Marino et al. 2017; Sezestre et al. 2019), which is thought to be the main source of zodiacal dust in the solar system (Nesvorný et al. 2010; Shannon et al. 2015; Poppe et al. 2019). Thus, observations of HZ dust have the potential to put constraints on the cometary activity in the system, providing insights into the dynamics of the outer regions (Bonsor et al. 2012, 2014; Faramaz et al. 2017; Marino et al. 2017) and the environmental conditions of potential rocky planets (cometary bombardment, delivery of water; Kral et al. 2018). Other scenarios such as a recent, catastrophic collision near the HZ (e.g., Lisse et al. 2012; Bonsor et al. 2013; Meng et al. 2014; Su et al. 2019) or local dust production in a massive belt of planetesimals near the HZ are likely less common, but the fact that systems dominated by such processes exist has important implications for the architecture and evolution of HZs. Their frequency is yet to be determined beyond the most extreme cases, but the existence of rare bright ones implies a population of more common faint ones (Kennedy & Wyatt 2013). While spatial dust structures may hinder exo-Earth imaging, studying them may also reveal the presence of otherwise currently undetectable HZ planets and help to determine their properties (Stark & Kuchner 2008; Ertel et al. 2012b; Shannon et al. 2015).

Detecting exozodiacal dust is challenging due to the small separation from its host star[19] and the dust temperature of a few 100 K, which means it emits predominantly in the mid-infrared

where it is outshone by the star. Photometric observations to detect the dust excess emission are limited to a sensitivity of a few per cent of the stellar emission due to flux calibration uncertainties and limitations in predicting the stellar photospheric flux. This limit is significantly higher than measured for all but the most extreme and rare excesses. Spectroscopic observations may slightly improve over this sensitivity if silicate emission features can be detected (Ballering et al. 2014). Detecting scattered light from dust very close to the star in visible-light aperture polarization measurements has been unsuccessful, which puts important constraints on the properties and origin of the hot, near-infrared-detected dust (Marshall et al. 2016). Interferometry is required to spatially resolve the thermal dust emission in the infrared and thus disentangle it from the host star. This has been done successfully for the hot dust using optical long-baseline interferometry in the near-infrared (Absil et al. 2006, 2013; Defrère et al. 2012a; Ertel et al. 2014a, 2016; Nuñez et al. 2017). In the mid-infrared where HZ dust is the brightest, nulling interferometry (Bracewell & MacPhie 1979; Hinz et al. 1998, 2000) has been used to suppress the bright, unresolved starlight and detect the faint, extended dust emission (Stock et al. 2010; Millan-Gabet et al. 2011; Mennesson et al. 2014; Ertel et al. 2018b).

In this paper, we present and statistically analyze the complete data set from the Hunt for Observable Signatures of Terrestrial planetary Systems (HOSTS) survey. We have observed a sample of 38 nearby stars using the nulling mode of the Large Binocular Telescope Interferometer (LBTI; Hinz et al. 2016). Our observations probed for HZ dust around the target stars with approximately five times better sensitivity than past observations. Thus, they provide the strongest direct constraints on the HZ dust contents of a sample of nearby planetary systems and the strongest statistical constraints for future exo-Earth imaging mission target stars.

We describe our observations and data reduction in Section 2. In Section 3, we present our basic results. We discuss our data quality and detection criteria (Section 3.1), and describe the conversion of the astrophysical null measurements to dust levels in units of "1 zodi," i.e., multiples of the vertical optical depth of the solar system's HZ dust (Section 3.2). A discussion of our results is presented in Section 4. We start with extracting and discussing basic detection statistics that we correlate with other parameters of the observed targets, such as stellar spectral type, age, and the presence of known cold dust (Section 4.1). We discuss the prospects of more detailed studies of our detections based on our available data and follow-up observations with the LBTI in Section 4.2. In Section 5, we describe a deeper statistical analysis of our data that provides the strongest possible constraints on the typical zodi level around future exo-Earth imaging targets (Section 5.1), discuss the implications of our results for future exo-Earth imaging missions (Section 5.2), and outline a path forward to further improve the LBTI's sensitivity and provide even stronger constraints from a revived HOSTS survey (Section 5.3). Our conclusions are presented in Section 6.

2. Observations and Data Reduction

The observations for the HOSTS survey were carried out with the LBTI (Hinz et al. 2016) following the strategy outlined in detail by Ertel et al. (2018b). We used nulling interferometry in the N' filter ($\lambda_c = 11.11$ μm, $\Delta\lambda = 2.6$ μm) to combine the light from the two 8.4 m apertures of the LBT and to suppress

---

[19] A separation of 1 au at a typical distance of 10 pc for nearby stars corresponds to $0\rlap{.}{''}1$.

the light from the central star through destructive interference. The total flux transmitted through the interferometric null was measured on our Nulling-Optimized Mid-Infrared Camera (NOMIC; Hoffmann et al. 2014) detector and compared to a photometric observation of the target star to determine the null leak (fraction of light transmitted). Nodding and aperture photometry were used to subtract the variable telescope and sky background. Each observation of a science target (SCI) was paired with an identical observation of a calibration star (CAL) to determine the instrumental null leak (nulling transfer function, the instrumental response to a point source). The difference between the total null leak and the instrumental null leak is the astrophysical null N_{as}, i.e., the source flux transmitted through the instrument due to spatially resolved emission. Multiple such calibrated science observations were executed (typically two to four) and typically grouped in sequences of CAL–SCI–SCI–CAL for observing efficiency.

Science targets were selected according to target observability and priority from the full HOSTS target list compiled by Weinberger et al. (2015). This list consists of nearby, bright ($N > 1$ Jy) main-sequence stars without known close binary companions (within $1\!''\!5$). Because of their low luminosities, stars with late spectral types need to be close to pass our brightness limit and are thus relatively rare in our sample. The sample can be separated into early-type stars (spectral types A to F5), around which our observations are most sensitive, and Sun-like stars (spectral types F6 to K8), which are preferred targets for future exo-Earth imaging missions. The observed stars are listed with their relevant properties and observing dates in Table 1. About half of the stars selected by Weinberger et al. (2015) have been observed; the observed stars are representative of the full list with no significant additional biases other than target observability during the observing nights when nulling was possible (see below).

Calibrators were selected following Mennesson et al. (2014) using the catalogs of Bordé et al. (2002) and Mérand et al. (2005), supplemented by stars from the Jean–Marie Mariotti Center Stellar Diameter Catalog and the SearchCal tool (both Chelli et al. 2016) where necessary. Multiple calibrators were selected for each science target so that the same calibrator was typically not used repeatedly for the same science target in order to minimize systematic errors due to imperfect knowledge of the calibrator stars (potential binarity or circumstellar emission, uncertain diameter).

Observations were carried out in queue mode together with a variety of other observing programs using the LBTI, including high-contrast direct imaging (e.g., Stone et al. 2018b) and integral field spectroscopic observations (e.g., Stone et al. 2018a; Briesemeister et al. 2019). This increased the pool of nights to choose from for the nulling observations, which are very demanding in terms of weather conditions. A total of 10 nights of observing time per observing semester was allocated for the HOSTS survey over the 2016B to 2018A semesters (40 nights total), of which typically three to four nights per semester were used successfully while the rest was largely lost due to unsuitable weather conditions (during which we often executed other, less demanding projects from our observing queue).

Data reduction followed the strategy outlined by Defrère et al. (2016) with minor updates as described by Ertel et al. (2018b). After a basic reduction of each frame (nod subtraction, bad pixel correction), aperture photometry was performed on each single frame. Three different photometric apertures were used to (1) cover one resolution element of the single-aperture point-spread function (PSF), to (2) optimize the photon- and read-noise-limited S/N for extended emission analogous to the solar system zodiacal dust, and to (3) include all plausible extended N band dust emission from the system. These apertures were discussed and motivated in detail by Ertel et al. (2018b). They respectively have radii of 8 pix (143 mas), 13 pix (233 mas), and the EEID[20] plus one FWHM of the single-aperture PSF (EEID + 313 mas, "conservative aperture"). The raw null depths and their uncertainties were determined using the null self-calibration method (NSC; Hanot et al. 2011; Mennesson et al. 2011; Defrère et al. 2016; Mennesson et al. 2016), combining all frames recorded within a given nod for a statistical analysis. These measurements within an observing sequence of a science target were then combined, and the corresponding calibrator observations were used to calibrate the null measurements. These calibrated astrophysical null measurements for each aperture and each science target are listed in Table 2. All raw and calibrated HOSTS data are available to the public through the LBTI Archive (http://lbti.ipac.caltech.edu/).

3. Results

3.1. Data Quality and Detection Criteria

The astrophysical null and zodi measurements derived from the HOSTS survey are listed in Table 2. Figure 1 shows the astrophysical null measurements and sensitivities reached for all stars and the three apertures used. The distributions of the significance N_{as}/σ_N of the measurements (the ratio of the calibrated, astrophysical null measurement N_{as} to its measurement uncertainty σ_N) are generally well behaved, consistent with a Gaussian distribution around a significance of $N_{as}/\sigma_N = 0$ and a tail of detections at $N_{as}/\sigma_N > 3$. This can be expected for a sample in which a fraction of stars have no detectable excesses, while the other stars do have significant excess. The standard deviation of the Gaussian component (measured for stars with $N_{as}/\sigma_N < 3$) is $\sim$1.3, slightly larger than the expected value of 1. This may indicate either that among the stars without significant null excess there are still stars with tentative excesses, or that we slightly underestimate our measurement uncertainties. While the former can generally be expected, the latter is supported by the symmetrical distribution of nondetections around $N_{as}/\sigma_N = 0$. The distribution of the measurement uncertainties is well behaved, with a sharp peak at low uncertainty and a tail toward higher uncertainties for stars observed under less suitable conditions or for which a smaller amount of data was obtained than for others. As expected from background photon and detector read noise, the median null uncertainty increases with aperture size. The larger scatter for the conservative aperture can be explained by the fact that this aperture is optimized for each star, and thus, its size (and with it the photon and read noise of the measurement) changes from target to target. Based on these arguments, we define a significant excess detection as a star for which we measure $N_{as}/\sigma_N > 4$ in at least one aperture.

In principle, any of our detections could be caused by the presence of an unknown binary companion instead of a dust

Table 1
Observed Targets and Relevant Stellar Parameters

HD number	Name	Spectral Type	V (mag)	K (mag)	N'[a] (Jy)	d (pc)	Age (Myr)	EEID[b] (mas)	fIR/nIR excess	Excess references	# SCI[c]	PA range[d] (deg)	Dates observed[e]
Sensitivity-driven sample (Spectral types A to F5)[f]:													
33111	β Eri	A3 IV	2.782	2.38	3.7	27.4	761	248	N/N	1, 2, 3	2	[22, 37]	2017 Feb 10
38678	ζ Lep	A2 IV-V	3.536	3.31	2.1	21.6	587	176	Y/Y	4, 5	1/6	[6, 8]	2017 Dec 23
81937	23 UMa	F0 IV	3.644	2.73	2.6	23.8	1172	168	N/–	6	1	[−158, 175][N]	2016 Nov 15
											2	[−124, −144][N]	2017 Feb 11
											2	[173, 159][N]	2018 Mar 30
95418	β UMa	A1 IV	2.341	2.38	4.2	24.5	404	316	Y/N	5, 7	4	[−145, 168][N]	2017 Apr 3
97603	δ Leo	A5 IV	2.549	2.26	3.9	17.9	718	278	N/N	1, 2, 5	2	[−54, −46]	2017 Feb 10
											2	[21, 52]	2017 May 12
102647	β Leo	A3 V	2.121	1.92	6.9	11.0	45	336	Y/Y	5, 7	2	[41, 58]	2015 Feb 8
103287	γ UMa	A0 IV	2.418	2.43	3.7	25.5	334	308	N/–	1, 2, 7	2	[−163, 168][N]	2017 Apr 6
											2	[128, 113][N]	2017 May 1
106591	δ UMa	A2 V	3.295	3.10	2.0	24.7	234	199	N/N	1, 2, 5	2	[−113, 167][N]	2017 Feb 9
											2	[150, 133][N]	2017 May 21
											3	[171, 118][N]	2018 May 25
108767	δ Crv	A0 IV	2.953	3.05	2.3	26.6	175	251	N/Y	1, 2, 3	2	[−20, −7]	2017 Feb 10
109085	η Crv	F2 V	4.302	3.54	1.8	18.3	1433	125	Y/N	8, 9	3	[−5, 32]	2014 Feb 12
128167	σ Boo	F4 V	4.467	3.47	1.4	15.8	1703	117	Y[g]/N	1,5	1	[−50, 70]	2017 Apr 3
											2	[−74, −66]	2017 Apr 6
129502	μ Vir	F2 V	3.865	2.89	2.6	18.3	1753	151	N/N	1, 3	3	[−26, 4]	2017 Feb 10
172167	α Lyr	A0 V	0.074	0.01	38.6	7.68	428	916	Y/Y	5, 7	2	[−106, −125][N]	2017 Apr 6
											2	[−89, −100][N]	2018 Mar 28
187642	α Aql	A7 V	0.866	0.22	21.6	5.13	739	570	N/Y	1, 2, 5, 10	2	[−52, 20][N]	2017 May 12
203280	α Cep	A8 V	2.456	1.85	7.0	15.0	958	294	N/Y	1, 2, 5, 10	1	[130, 121][N]	2016 Oct 16
Sun-like stars sample (Spectral types F6 to K8)[f]:													
9826	υ And	F9 V	4.093	2.84	2.4	13.5	4000	136	N/N	5, 11	2	[−118, 158][N]	2017 Dec 20
10476	107 Psc	K1 V	5.235	3.29	2.0	7.53	4990	90	N/N	1, 5, 11, 12	1	[−20, 12]	2016 Nov 14
											2	[−40, 22]	2016 Nov 16
10700	τ Cet	G8 V	3.489	1.68	5.4	3.65	5800	182	Y/Y	5, 13	2	[5, 29]	2018 Jan 5
16160	GJ 105 A	K3 V	5.815	3.45	1.5	7.18	6100	73	N/–	1, 11, 12	1	[9, 19]	2016 Nov 15
22049	ϵ Eri	K2 V	3.721	1.67	7.4	3.22	600	172	Y/Y	8, 14	2	[−4, 16]	2017 Dec 20
											2	[−19, 4]	2017 Dec 23
30652	1 Ori	F6 V	3.183	2.08	4.8	8.07	1200	205	N/N	1, 5, 11, 12	2	[0, 25]	2017 Feb 9
											2	[5, 23]	2017 Dec 20
34411	λ Aur	G1 V	4.684	3.27	1.8	12.6	7700	105	N/–	11, 15	2	[101, 83] N	2017 Jan 29
48737	ξ Gem	F5 IV-V	3.336	2.13	4.3	18.0	2000	196	–/N	5	2	[0, 19]	2016 Nov 14
											1	[−44, 21]	2016 Nov 15
78154	13 UMa	F7 V	4.809	3.53	1.2	20.4	4900	99	N/–	1	2	[−168, 163] N	2018 Mar 29
											1	[141, 127] N	2018 Mar 30
88230	GJ 380	K8 V	6.598	3.21	1.9	4.87	1200	65	N[h]/–	16	2	[−143, −167] N	2017 Apr 6
89449	40 Leo	F6 IV-V	4.777	3.65	1.1	21.4	3100	98	N/–	1,6	2	[−58, −16] N	2017 Feb 9
102870	β Vir	F9 V	3.589	2.31	4.3	10.9	4400	173	N/N	5, 11	2	[−25, −3]	2017 Dec 20
											2	[13, 26]	2018 Mar 30
120136	τ Boo	F6 IV	4.480	3.36	1.7	15.6	1300	114	N/N	3, 11, 15	2	[28, 57]	2017 May 12
											2	[10, 38]	2018 Mar 30
126660	θ Boo	F7 V	4.040	2.81	3.1	14.5	500	147	N[i]/–	1, 11, 12	1	[−170, 164] N	2017 Feb 9
											2	[−170, 152] N	2017 Apr 11
											2	[−158, 176] N	2018 May 23
141004	λ Ser	G0 IV-V	4.413	2.98	2.4	12.1	5300	121	N/N	1, 5, 12, 17	2	[7, 24]	2017 May 1
142373	χ Her	G0 V	4.605	3.12	2.0	15.9	6210	111	N/N	1, 5, 6, 12	3	[131, 99] N	2017 Apr 11

Table 1
(Continued)

HD number	Name	Spectral Type	V (mag)	K (mag)	N′[a] (Jy)	d (pc)	Age (Myr)	EEID[b] (mas)	fIR/nIR excess	Excess references	# SCI[c]	PA range[d] (deg)	Dates observed[e]
142860	γ Ser	F6 IV	3.828	2.63	2.9	11.3	4600	151	N/N	1, 5, 12, 15	2	[−29, −8]	2017 Apr 6
											2	[−30, 12]	2017 May 21
157214	72 Her	G0 V	5.381	3.84	1.0	14.3	6900	79	N/–	11	2	[−84, −86]	2018 May 23
											2	[−84, −85]	2018 May 25
173667	110 Her	F6 V	4.202	3.03	2.2	19.2	2200	131	Y[j]/Y	5, 11, 16	2	[−56, −31]	2017 Apr 8
											3	[−63, −50]	2018 Mar 30
185144	σ Dra	G9 V	4.664	2.83	2.7	5.76	3500	113	N/N	5, 11, 15	2	[−143, −163] N	2017 May 1
201091	61 Cyg A	K5 V	5.195	2.36	4.4	3.49	7000	106	N/N	5, 13	2	[−92, −115] N	2018 May 23
											2	[−92, −100] N	2018 May 25
215648	ξ Peg A	F6 V	4.203	2.90	2.2	16.3	5000	132	N/N	1, 6, 12	1	[20, 30]	2016 Nov 14
											2	[4, 25]	2016 Nov 16
222368	ι Psc	F7 V	4.126	2.80	2.4	13.7	5000	137	N/–	6	2	[−33, 37]	2017 Nov 10

Notes. Magnitudes are given in the Vega system.
[a] Predicted flux in NOMIC N' filter.
[b] Earth Equivalent Insolation Distance (Weinberger et al. 2015).
[c] Number of calibrated science pointings obtained.
[d] Approximate parallactic angle (PA) range covered by the observations. In practice, the PA coverage in this range is not uniform due to changing sky rotation and observations being unevenly distributed in time. Northern targets are marked by an "N" as they culminate at the $-180° \equiv 180°$ discontinuity of the PA rather than $0°$.
[e] All data, including auxiliary information such as weather conditions, exact observing time, and hour angle coverage, are available in the HOSTS archive (http://lbti.ipac.caltech.edu/).
[f] Section 2.
[g] Misclassified by Gáspár et al. (2013) as no excess.
[h] Cold excess (Eiroa et al. 2013) likely background contamination (Gáspár & Rieke 2014).
[i] Tentative detection at 2.5σ (Montesinos et al. 2016), may have a faint excess.
[j] Marginal excesses from *Spitzer* at 70 μm (Trilling et al. 2008) and *Herschel* at 70 μm and 100 μm excesses (Eiroa et al. 2013; Marshall et al. 2013); taken together likely a faint excess. References are spectral type: SIMBAD; V magnitude: Kharchenko et al. (2007); K magnitude: Gezari et al. (1993) and the Lausanne photometric database (http://obswww.unige.ch/gcpd/gcpd.html); N-band flux and EEID: Weinberger et al. (2015); distance: van Leeuwen (2007); excess: (1) Gáspár et al. (2013), (2) Thureau et al. (2014), (3) Ertel et al. (2014a), (4) Mannings & Barlow (1998), (5) Absil et al. (2013), (6) Beichman et al. (2006), (7) Su et al. (2006), (8) Absil et al. (2006), (9) Aumann (1988), (10) Rieke et al. (2005), (11) Trilling et al. (2008), (12) Montesinos et al. (2016), (13) Greaves et al. (2004), (14) Aumann (1985), (15) Lawler et al. (2009), (16) Eiroa et al. (2013), (17) Koerner et al. (2010).

disk. However, most of our targets have been observed at a range of parallactic angles. A binary companion would rotate across the transmission pattern in and out of the transmissive fringes with parallactic angle rotation. This will typically result in a variation between full null excess (companion on transmissive fringe) and zero null excess (companion on dark fringe), while limited field rotation may result in any scenario in between these extrema depending on the exact configuration of a binary system. Although the limited excess significance for most of our detections prevents a definitive conclusion, binarity is an unlikely scenario. Many of our targets have also been observed with high-contrast imaging observations searching for giant planets and no detections of binary companions have been reported (e.g., Stone et al. 2018b; Mawet et al. 2019).

We have detected significant excesses around 10 stars out of the total of 38 stars observed. In fact, all of these stars show excesses $N_{as}/\sigma_N > 5$ and/or have been detected combining consistent data from at least two independent observations (i.e., in at least two different nights). We thus consider all these detections robust.

3.2. Null-to-zodi Conversion

A detailed description of the modeling strategy for the HOSTS data has been presented by Kennedy et al. (2015) and updated by Ertel et al. (2018b). In the Appendix, we provide a cookbook on how to compare a disk model to our null measurements for general model fitting.

For the conversion from astrophysical null measurements to dust levels (zodis), we used the model presented by Kennedy et al. (2015). It describes a radial dust surface density distribution analogous to the solar system's zodiacal dust (Kelsall et al. 1998), scaled in size with the square root of the host star's luminosity. We scale the dust surface density (vertical geometrical optical depth) of this model to 7.12×10^{-8} at the EEID, equal to the surface density of the zodiacal dust at 1 au from the Sun (Kelsall et al. 1998). This defines the unit of 1 zodi, which we use to quantify the HZ dust levels around our target stars.

Note that the unit of 1 zodi is a unit of vertical geometrical optical depth (surface density) of the dust in a star's HZ. It thus does not depend on the observing wavelength or emission mechanism. We emphasize here that there are limitations to this approach related to the simplifications of the model and the likely variety of planetary system and dust architectures around our target stars. In particular, if the spectral shape of the dust emission is different from that of the solar system, applying our method of measuring a star's zodi level to observations at a different wavelength would yield a different zodi measurement

Table 2
Basic Stellar Parameters, Astrophysical Null Measurements, and Zodi Levels for the Stars Observed by the HOSTS Survey

Aperture →		8 pix		13 pix			Conservative						
HD number	Name	N_{as} (%)	σ_N (%)	N_{as} (%)	σ_N (%)	r_{ap} (pix)	N_{as} (%)	σ_N (%)	Aperture for zodi	$N_{as,1}$ (%)	z (zodi)	σ_z (zodi)	z/σ_z
Sensitivity-driven sample (Spectral types A to F5):													
33111	β Eri	−0.004	0.110	0.168	0.119	18	0.372	0.176	13 pix	5.27×10^{-3}	31.9	22.6	1.4
38678	ζ Lep	1.795	0.205	1.609	0.313	25	3.496	0.214	cons.	5.77×10^{-3}	605.8	37.2	16.3
81937	23 UMa	−0.065	0.061	−0.032	0.078	25	−0.135	0.142	13 pix	3.31×10^{-3}	−9.8	23.5	−0.4
95418	β UMa	0.920	0.055	1.019	0.060	33	1.655	0.102	13 pix	7.45×10^{-3}	136.7	8.0	17.1
97603	δ Leo	0.028	0.051	0.033	0.055	32	−0.013	0.143	13 pix	6.10×10^{-3}	5.5	9.0	0.6
102647	β Leo	0.470	0.050	0.420	0.054	32	1.160	0.333	8 pix	4.54×10^{-3}	103.5	11.0	9.4
103287	γ UMa	−0.037	0.033	0.003	0.031	34	0.083	0.080	13 pix	8.00×10^{-3}	0.4	3.9	0.1
106591	δ UMa	0.453	0.065	0.503	0.082	28	0.924	0.144	8 pix	5.38×10^{-3}	84.2	12.1	7.0
108767	δ Crv	−0.333	0.131	−0.243	0.199	26	0.933	0.365	13 pix	9.01×10^{-3}	−26.9	22.1	−1.2
109085	η Crv	4.410	0.350	4.580	0.460	24	4.710	0.890	8 pix	2.26×10^{-3}	1952.3	154.9	12.6
128167	σ Boo	−0.019	0.096	−0.006	0.118	22	0.417	0.252	13 pix	2.46×10^{-3}	−2.3	48.0	0.0
129502	μ Vir	−0.006	0.092	0.183	0.110	25	0.192	0.198	13 pix	2.64×10^{-3}	69.2	41.8	1.7
172167	α Lyr	0.055	0.034	0.123	0.038	37	0.392	0.089	cons.	1.18×10^{-2}	33.2	7.5	4.4
187642	α Aql	−0.032	0.166	0.217	0.192	47	−0.995	0.356	13 pix	4.16×10^{-3}	52.1	46.3	1.1
203280	α Cep	−0.301	0.376	−0.233	0.182	18	−0.075	0.266	13 pix	3.91×10^{-3}	−59.6	46.6	−1.3
Sun-like stars sample (Spectral types F6 to K8):													
9826	υ And	−0.245	0.079	−0.287	0.090	24	−0.276	0.169	13 pix	2.20×10^{-3}	−130.3	40.8	−3.2
10476	107 Psc	−0.028	0.083	−0.027	0.122	21	0.154	0.181	13 pix	9.45×10^{-4}	−28.3	129.4	−0.2
10700	τ Cet	0.074	0.079	−0.014	0.084	27	−0.022	0.139	13 pix	1.90×10^{-3}	−7.5	43.8	−0.2
16160	GJ 105 A	0.228	0.232	−0.227	0.239	18	0.538	0.363	13 pix	7.12×10^{-4}	−319.2	336.2	−0.9
22049	ϵ Eri	0.144	0.068	0.240	0.066	27	0.463	0.087	cons.	1.56×10^{-3}	296.6	55.6	5.3
30652	1 Ori	0.078	0.098	0.107	0.101	28	0.016	0.165	13 pix	2.78×10^{-3}	38.4	36.2	1.1
34411	λ Aur	−0.210	0.095	−0.108	0.079	22	0.041	0.136	13 pix	1.57×10^{-3}	−69.1	50.6	−1.4
48737	ξ Gem	0.048	0.099	0.124	0.098	27	0.057	0.229	13 pix	2.73×10^{-3}	45.4	35.9	1.3
78154	13 UMa	0.369	0.102	0.398	0.144	22	0.028	0.181	13 pix	1.89×10^{-3}	210.1	75.8	2.8
88230	GJ 380	−0.111	0.059	−0.077	0.056	20	−0.189	0.087	13 pix	4.19×10^{-4}	−184.7	134.2	−1.4
89449	40 Leo	0.238	0.263	−0.018	0.290	21	1.278	0.578	13 pix	2.19×10^{-3}	−8.4	132.5	−0.1
102870	β Vir	−0.069	0.039	−0.054	0.049	26	−0.172	0.098	13 pix	2.11×10^{-3}	−25.5	23.0	−1.1
120136	τ Boo	0.111	0.108	−0.112	0.111	22	0.300	0.216	13 pix	2.09×10^{-3}	−53.8	53.0	−1.0
126660	θ Boo	0.280	0.052	0.329	0.066	24	0.441	0.083	8 pix	1.89×10^{-3}	148.2	27.7	5.4
141004	λ Ser	0.015	0.036	0.025	0.047	23	−0.107	0.117	13 pix	1.68×10^{-3}	15.1	28.1	0.5
142373	χ Her	−0.063	0.052	0.112	0.061	22	0.071	0.083	13 pix	1.63×10^{-3}	69.1	37.2	1.9
142860	γ Ser	0.037	0.044	−0.009	0.058	25	0.023	0.079	13 pix	2.35×10^{-3}	−3.7	24.6	−0.2
157214	72 Her	0.713	0.146	0.600	0.173	20	0.674	0.193	8 pix	1.21×10^{-3}	587.5	120.5	4.9
173667	110 Her	0.152	0.070	0.194	0.087	24	0.621	0.120	cons.	2.64×10^{-3}	234.9	45.4	5.2
185144	σ Dra	0.027	0.052	−0.075	0.071	22	−0.096	0.096	13 pix	1.25×10^{-3}	−60.2	56.9	−1.1
201091	61 Cyg A	0.060	0.053	0.047	0.050	22	0.126	0.231	13 pix	7.00×10^{-4}	66.7	71.3	0.9
215648	ξ Peg A	0.154	0.121	0.226	0.167	23	0.198	0.214	13 pix	2.22×10^{-3}	101.7	75.0	1.4
222368	ι Psc	−0.099	0.127	0.016	0.133	23	−0.062	0.271	13 pix	2.24×10^{-3}	7.2	59.4	0.1

Note. Table columns are N_{as}—astrophysical null measurement in a given aperture; σ_N—uncertainty of the null measurement; r_{ap}—radius of the conservative aperture; $N_{as,1}$—astrophysical null expected from 1 zodi; z—final zodi measurement; σ_z—uncertainty on final zodi measurement; z/σ_z—significance of zodi measurement.

result. For detailed discussions of the shortcomings of our approach and how they are at least in part mitigated by the optimized design of the LBTI, we refer to Kennedy et al. (2015) and Ertel et al. (2018b).

The usually unknown orientation of the potential dust disk (inclination and position angle) were randomized, and the response of the LBTI to all possible orientations was used to compute a most likely null-to-zodi conversion factor (the astrophysical null $N_{as,1}$ expected from a 1 zodi disk; Table 2). As pointed out by Ertel et al. (2018b), in practice the uncertainty from the disk orientation is negligible compared to the null measurement uncertainty due to the range of hour angles over which each target has been observed. Correction

factors for the finite aperture size were computed from the same model by convolving the model image of the transmitted dust emission with the single-aperture PSF of the observations and dividing the total predicted null excess from the model by the null excess predicted in a given aperture. For detected excesses, we converted the astrophysical null measurement from the aperture that yields the most significant detection (Table 2) to a zodi level. For nondetections, we used the measurement based on the noise-optimized aperture assuming a dust distribution analogous to the solar system's zodiacal dust. All our detections agree with this assumption within the measurement uncertainties. We find a median 1σ sensitivity of 23 zodis for early-type stars and 48 zodis for Sun-like stars.
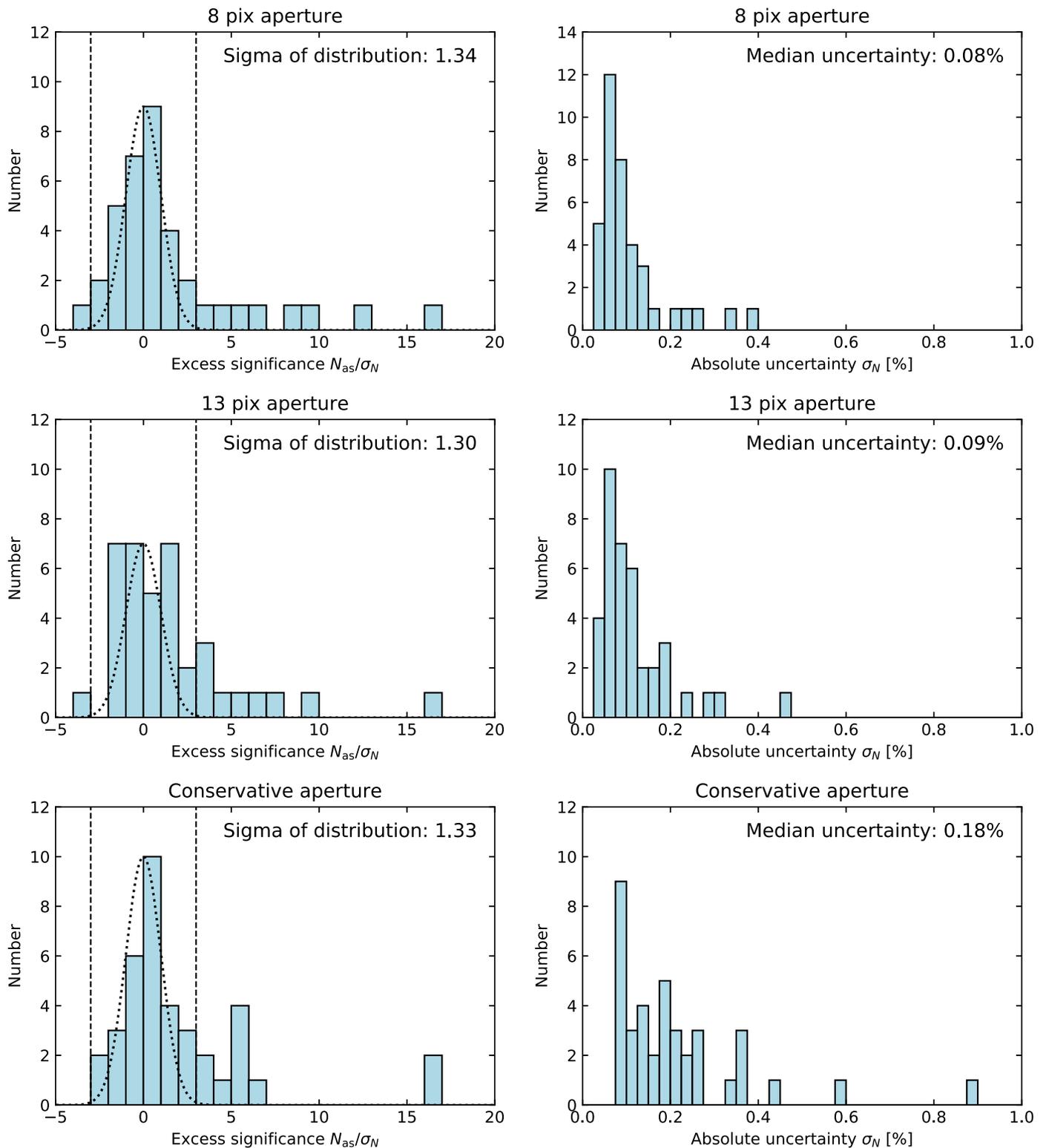
Figure 1. Histograms of astrophysical null measurements and uncertainties for all host survey observations.

4. Discussion

In this section, we interpret our results. We first discuss the detection rates and their correlations with other system parameters and hypothesize about the sources of the correlations (Section 4.1). We then briefly discuss the potential for further observations and detailed analyses of our strong detections to better understand these individual systems (Section 4.2). A statistical analysis to derive the typical zodi level around the Sun-like stars and a discussion of the implications for future exo-Earth imaging, including the merit

Table 3
Subsamples, LBTI Excess Detections, and Rates vs. Auxiliary Data

	Early type	Sun-like	All
All stars	6 of 15 $40^{+13}_{-11}\%$	4 of 23 $17^{+10}_{-5}\%$	10 of 38 $26^{+8}_{-6}\%$
Cold dust	5 of 6 $83^{+6}_{-23}\%$	2 of 3 $67^{+15}_{-28}\%$	7 of 9 $78^{+8}_{-18}\%$
No cold dust	1 of 9 $11^{+18}_{-4}\%$	2 of 19 $11^{+11}_{-4}\%$	3 of 28 $11^{+9}_{-3}\%$
Hot excess	3 of 6 $50^{+18}_{-18}\%$	1 of 2 $50^{+25}_{-25}\%$	4 of 8 $50^{+16}_{-16}\%$
No hot excess	3 of 7 $43^{+18}_{-15}\%$	1 of 13 $8^{+14}_{-3}\%$	4 of 20 $20^{+12}_{-6}\%$
Young[a]	5 of 8 $63^{+13}_{-18}\%$	3 of 12 $25^{+15}_{-8}\%$	…
Old[a]	1 of 8 $13^{+20}_{-4}\%$	1 of 12 $8^{+15}_{-3}\%$	…
Young w/o ζ Lep	4 of 7 $57^{+15}_{-18}\%$	…	…
Old w/o η Crv	0 of 7 $0^{+21}_{-0}\%$	…	…

Notes. The presence or absence of cold dust and hot excess for our target stars is indicated in Table 1.
[a] Stars younger or older than the median age of their respective spectral-type bin. The star with the median age in each subsample (a nondetection in each case) was included in both the young and old group, which is why the sum of young and old stars is one larger than the total number of stars.

of more observations with an improved sensitivity that can realistically be achieved by moderate instrument upgrades to the LBTI, is presented in Section 5.

4.1. Detection Statistics and Correlation with Other System Parameters

We detect significant excesses around 10 stars out of the total of 38 stars observed. These detections include β Leo (D. Defrère et al. 2020, in preparation) and η Crv (Defrère et al. 2015). We previously excluded those two targets from the statistical analysis of an early subset of HOSTS observations in Ertel et al. (2018b), because the data on them were taken during commissioning time, not as part of the unbiased HOSTS survey. Here we assume that toward the end of the HOSTS survey, as the number of available targets that had not yet been observed decreased, both stars would have been observed by the unbiased survey if they had not been observed as commissioning targets. They are thus now considered part of the unbiased survey. We will see that our detection statistics are consistent with these from Ertel et al. (2018b), so no significant bias is introduced from including or excluding these two stars.

The basic detection statistics for different subsamples of targets are summarized in Table 3. Our sample size is limited, and any statistical analysis is affected by large statistical uncertainties and small number statistics. We illustrate this by displaying binomial uncertainties with our detection rates. In addition, while the accuracy of our null measurements is independent of stellar spectral type, it is not the same for every star due to differences in data quality and quantity of individual targets. Moreover, our sensitivity to HZ dust is limited (as quantified by the sensitivity to dust in units of zodi) and
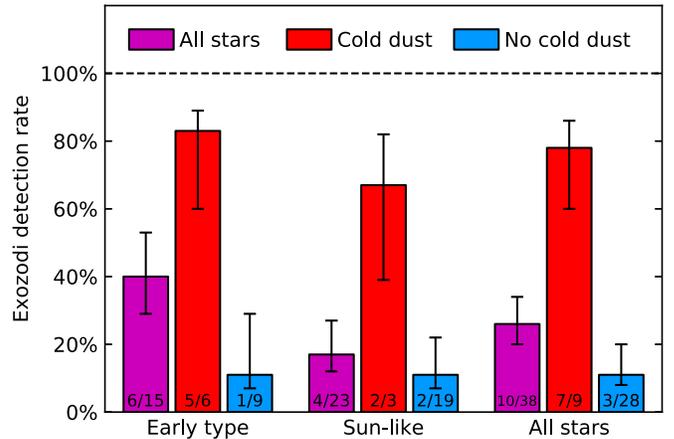
Figure 2. Histogram of HZ dust detection rates with respect to stellar spectral type and the presence of a detected, cold debris disk. The correlation between detection rate and spectral type is likely related to a sensitivity bias (Section 4.1). The correlation between detection rate and presence of cold dust is likely of astrophysical origin and found to be significant for early-type stars, while no conclusion can be drawn for Sun-like stars. The number of stars and detections in each subsample is indicated at the bottom of the corresponding bar.

decreases from earlier to later stellar spectral types (Kennedy et al. 2015). As a consequence, our detection rates cannot readily be converted into occurrence rates. Caution must be exercised when interpreting our detection rates, and any theoretical work predicting occurrence rates of exozodiacal dust needs to be compared to our observations for the individual stars directly rather than the detection rates. Such theoretical work is beyond the scope of the present paper. We thus limit ourselves in the following to a qualitative discussion of our detection rates and compare them to a range of other properties of the systems to search for correlations.

4.1.1. No Correlation with Stellar Spectral Type

Our detection statistics with respect to stellar spectral type are shown in Figure 2. We find a higher overall detection rate for early-type stars than for Sun-like stars of $40^{+13}_{-11}\%$ and $17^{+10}_{-5}\%$, respectively. Closer investigation, however, shows that this trend simply illustrates the dominant bias in our survey: it can be explained entirely by the spectral-type dependence of the LBTI's sensitivity. If we observed the zodi levels z measured around our early-type stars with the sensitivity σ_z to HZ dust of our Sun-like stars, we would expect a detection rate of 18% (4 of 23 stars), identical to our observed detection rate for Sun-like stars. We thus see no evidence in our data of a correlation of the occurrence rate or amount of HZ dust with stellar spectral type.

4.1.2. No Correlation with Stellar Age

Figure 3 shows the zodi levels of our targets versus stellar age. Ages for the Sun-like stars were taken from the compilations by Gáspár et al. (2013) and Sierchio et al. (2014). Four of the stars had relatively weak determinations in those works: 13 UMa, 40 Leo, 61 CygA, and ι Psc. We checked the ages for them against all relevant work since those papers were published and confirmed them for three, but a significantly different age of 7.0 Gyr has been found for 61 CygA by asteroseismology (Metcalfe et al. 2015) and adopted here. Ages for the early-type stars are based on the
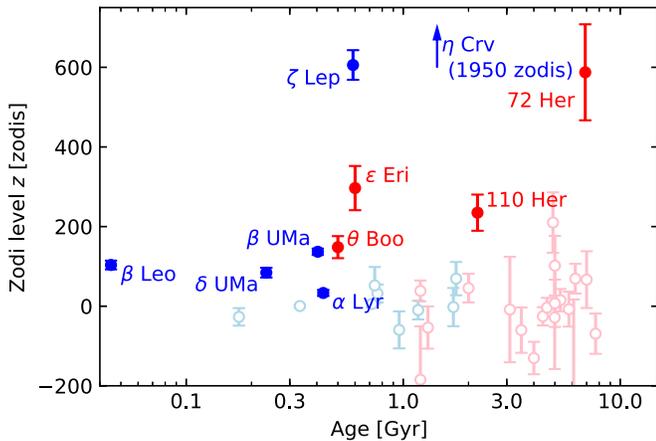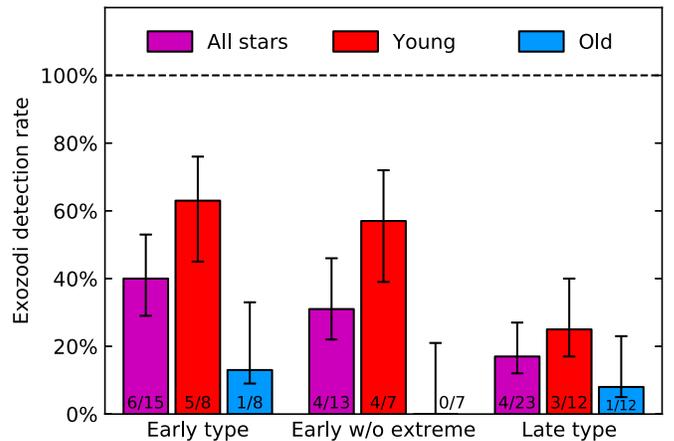
Figure 3. Age distribution of our target stars and the corresponding zodi measurements. Blue dots are for early-type stars, red ones for Sun-like stars. Filled symbols are for LBTI detections, and open, faint circles are for nondetections.

Figure 4. Detection rates with respect to the stellar age measured with respect to the median age of the sample a star belongs to. The visible trends can be attributed to a sensitivity bias (Section 4.1). The number of stars and detections in each subsample is indicated at the bottom of the corresponding bar. The star with the median age in each subsample (a nondetection in each case) was included in both the young and old group, which is why the sum of young and old stars is one larger than the total number of stars.

modes in the 1D fits by David & Hillenbrand (2015). Their determinations were from isochrones, a technique that loses resolution for young stars near the zero age main sequence. We therefore checked such stars against other sources, finding general consistency except for β Leo, which Zuckerman (2019) finds to be a member of the Argus moving group with an age of 40–50 Myr. Except for this latter case, where we adopted the moving group age, we used the ages from David & Hillenbrand (2015), so our comparisons would be on a consistent scale.

We see in Figure 3 that the stars with detected LBTI excesses tend to be on the younger side of both the early-type and the Sun-like samples with a few exceptions. When separating the two samples into stars younger and older than the median age of the respective sample (718 Myr for the early-type stars, 4.6 Gyr for the Sun-like stars), we find a higher detection rate for younger stars than for older ones (Figure 4). This correlation becomes even clearer if we exclude the two potentially extreme cases of η Crv and ζ Lep. This is, however, likely a result of the same bias with stellar spectral type discussed in the previous section. Stars of earlier spectral type have shorter lifetimes than stars of later spectral type. Thus, the early-type and Sun-like stars older than the median age of their respective spectral-type samples are on average of later spectral types than stars younger than the median age of their respective spectral-type sample. As we are less sensitive for stars of later spectral type, we are on average less sensitive around stars in the older age bin than those in the younger age bin for each spectral-type sample. If we observed the excesses measured around the younger stars in each spectral-type sample with the sensitivities of the older stars in the same sample, we would expect detection rates that are marginally higher than—but entirely consistent with—those found for the older stars in each sample. Our small sample sizes prevent us, however, from seeing weak trends.

What is potentially more enlightening is the fact that the strongest excesses are not detected around the youngest stars. Among the early-type stars, the extreme excess around η Crv stands out due to the gigayear age of the star. The strong detection around the intermediate-age early-type star ζ Lep may or may not be another such case, but this large excess may also be caused by the proximity of the "cooler" dust in this system to the HZ (see Section 4.1.3). Among the Sun-like stars, the

cases of 72 Her and 110 Her at ages of several gigayears show that strong excesses may be present at any stellar age. Our detections at ages well beyond the $\sim$500 Myr lifetime of 24 μm excesses (Gáspár & Rieke 2014) suggest that the HZ dust in these systems is not linked to (decayed) asteroid belts, but may either arise from recent stochastic events or be linked to outer cold disks with longer lifetimes (Sierchio et al. 2014).

4.1.3. Strong Correlation with the Presence of Cold Dust

A strong correlation is visible in Figure 2 between the zodi detection rate and the presence of a known outer debris disk, detected photometrically through the far-infrared excess it produces around its host star. For the majority of our target stars with a known cold debris disk (seven of nine, 78^{+8}_{-18}%), we have also detected HZ dust, while only 3 of 28 stars without cold dust have detected HZ dust. We use the p-value from Fisher's exact test to evaluate if this correlation is significant. This is justified here despite the nonuniform sensitivity across our sample, because the sensitivity does not directly depend on the presence or absence of cold dust, so that this property does not introduce any bias. The correlation is strong for early-type stars ($p = 0.01$), while for Sun-like stars, the small number of three known debris disks in our sample prohibits a definite conclusion ($p = 0.07$). Observing stars with debris disks was not a priority of the HOSTS survey as such stars are unlikely to be first-choice targets for future exo-Earth imaging missions. Thus, the HOSTS samples were designed to be unbiased with respect to the presence of a cold debris disk. Because detectable debris disks are less common around Sun-like stars than around Early-type stars (Rieke et al. 2005; Montesinos et al. 2016), few stars in our Sun-like sample host such disks.

The correlation between our HZ dust detections and cold dust suggests that the origin of bright HZ dust is somehow connected to the presence of dust or minor bodies farther away from the star, e.g., through inward transport of dust due to PR drag (Wyatt 2005) or through dust delivery by comets (Nesvorný et al. 2010; Faramaz et al. 2017; Sezestre et al. 2019). It is, however, noteworthy that there are several detections of HZ dust in systems that do not have a detected

cold debris disk despite sensitive searches. This may suggest an alternative origin of the dust in these systems or that even cold debris disks that are too faint to be detected by current methods may still be a significant source of exozodiacal dust (Bonsor et al. 2012, 2014). It is important to point out here the two uncertain cases of θ Boo and 110 Her. Both systems have tentative detections of cold dust. We consider the far-infrared excess around 110 Her significant as it has been detected independently with *Spitzer* at 70 μm and *Herschel* at 70 μm and 100 μm, albeit with marginal significance, but consider θ Boo a nondetection with only a 2.5σ excess found by *Herschel*. Moving either of these two stars to the other category (cold excess versus no cold excess or vice versa) would not change our conclusions, but this illustrates that our analysis is limited not only by our own data but also the sensitivity of available debris disk surveys. The *Herschel* nondetection for 72 Her is not very constraining, with the strongest upper limit at only 40% of the stellar photosphere at 100 μm (Eiroa et al. 2013).

Figure 5 shows our measured zodi levels with respect to the temperature and fractional luminosity of the cold, outer debris disk (measured by a single modified blackbody fit to the spectral energy distribution of the far-infrared to millimeter excess measurements from the literature) for systems for which such a disk has been detected (7 out of our 10 detections, and 2 of our nondetections). We also add γ Oph from Mennesson et al. (2014). For stars with well-known warm belts inside the cold, outer belts, we include a point at the temperature of the warm belt, too. In addition, we plot model predictions of the amount of dust delivered to the HZ from outer belts at various temperatures and vertical optical depths under the influence of PR drag and collisions. The vertical optical depth of the dust in the HZ is computed following the equation (adapted from Wyatt 2005)

$$\tau_{\mathrm{HZ}} = \frac{\tau_0}{1 + 4 \times 10^4 \times \tau_0 \frac{278\,\mathrm{K}}{T_0} \left(\frac{L_\star^{0.25}}{M_\star^{0.5}}\right)\left(1 - \frac{T_0}{278\,\mathrm{K}}\right)}, \quad (1)$$

where T_0 and τ_0 are the temperature and vertical optical depth of the outer belt, respectively, and the stellar luminosity $L_\star$ and mass $M_\star$ are measured in solar units $L_\odot$ and $M_\odot$. The zodi level is then $z = \tau_{\mathrm{HZ}}/7.12 \times 10^{-8}$ following our definition in Section 3.2. This plot is analogous to Figure 10 in Mennesson et al. (2014), but plotted in zodi level instead of null depth and showing lines for various τ_0 (the lines in Mennesson et al. 2014 are shown for $\tau_0 = 10^{-4}$).

The predictions of the radial surface density distribution from this model are not identical to our solar zodi model used to convert our null measurements to zodis, which means that the two are not fully compatible (Section 3.2). However, both models have a fairly flat radial distribution throughout the HZ, and the design of the LBTI partly mitigates the impact of this discrepancy. The model has also been noted to underpredict the effect of collisions and thus overpredict the *N*-band flux of the disk (Kennedy & Piette 2015).

Despite those caveats, it is noteworthy that the model predicts most of our zodi measurements reasonably well. Because the model is unlikely to underpredict the HZ dust level, perhaps the strongest conclusions possible are that the HZ dust of η Crv cannot be explained by this model and that the HZ dust in the γ Oph and ϵ Eri systems is more likely to originate from the warmer belts than the outer, cold belt if
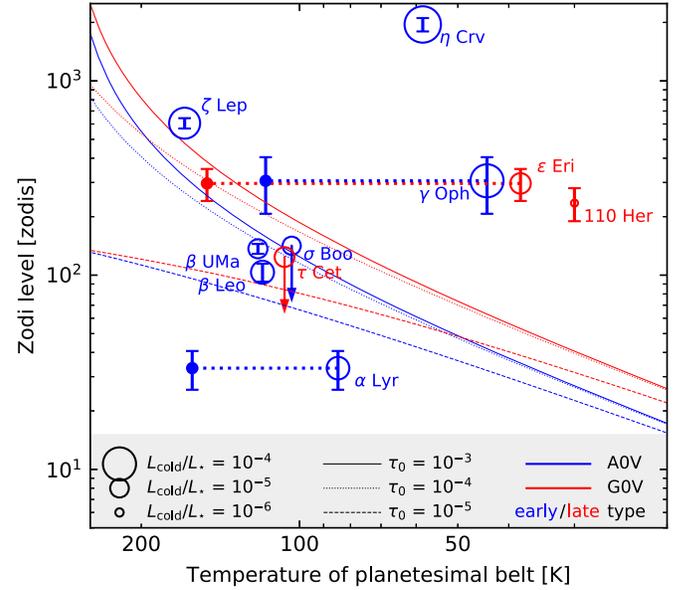
Figure 5. Zodi levels vs. temperature and luminosity of outer debris disks (where detected). Blue symbols are for early-type stars, red ones for Sun-like stars. Downward arrows indicate upper limits on zodi levels.

produced by PR drag (but stellar wind drag may affect the latter conclusion for low-luminosity stars; Reidemeister et al. 2011). Another potential outlier is 110 Her, but the detection of cold dust is very weak, and the constraints on warmer dust in the system are relatively poor (Eiroa et al. 2013). Thus, the system could be similar to ϵ Eri with an asteroid-belt analog that could be responsible for the large amounts of HZ dust. Furthermore, by comparison with the other detections around early A-type stars (β Leo, β UMa, and ζ Lep), the zodi level of α Lyr appears very low, which may suggest clearing by planets (Bonsor et al. 2018) in or outside the HZ if the dust in all of these systems is delivered by PR drag. Finally, our observations are consistent with the model predictions of closer outer belts producing higher zodi levels and little spectral-type dependence of this effect, but our small number statistics do not allow for strong conclusions.

4.1.4. No Connection with Hot Dust

We see no correlation between the presence of hot and HZ dust around early-type stars (Figure 6). The difference for Sun-like stars is not significant either ($p = 0.26$).

4.1.5. A Consistent Picture from the Present and Absent Trends

It is possible that we see the signs of different dust origins: for the early-type stars, to which we are the most sensitive, we may be able to detect the results of a delivery of material from an outer debris disk in some sort of continuous process. PR drag and a steady flow of comets from the outer system to the inner regions are potential mechanisms for this delivery, and both are likely at play to some degree depending on the architecture of each system. This would correlate with the presence of a cold disk and the delivered amount of dust would potentially decrease over time: Wyatt (2005) has shown that the HZ dust level for the PR drag scenario depends only weakly on the mass of the outer disk, and thus the effects of decreasing debris disk masses with age may be small (but measurable for low outer disk optical depths and warm outer disks; Figure 5).
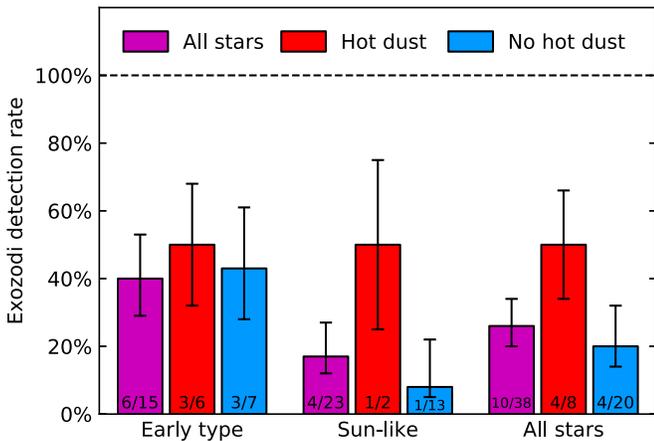
Figure 6. Histogram of HZ dust detection rates with respect to the presence of a detected near-infrared excess. The number of stars and detections in each subsample is indicated at the bottom of the corresponding bar.

Faramaz et al. (2017) have shown that comet delivery depends on the number of large bodies on suitable orbits in the outer system, which decreases over time due to their removal by both debris disk evolution and their ongoing delivery to the HZ. However, they have also found that HZ dust disks may be sustained over a gigayear timescale. On the other hand, there are potentially extreme systems such as η Crv. These systems may be produced by sporadic, catastrophic events, and as illustrated by the gigayear age of η Crv, these events may occur at least at this age. For Sun-like stars, we may typically be only sensitive enough to detect such extreme systems. Such events would also not necessarily originate from and correlate with the presence of a detectable debris disk, explaining our detections in systems without cold dust. Alternatively, Bonsor et al. (2012) and Marino et al. (2018) have suggested specific planetary system architectures that may support a high influx of comets.

These hypotheses may be tested observationally. Improving the sensitivity of the LBTI by a factor of 2 to 3 is realistic with moderate instrument upgrades (Section 5.3). This should allow for the detection of more of the supposedly continuously supplied HZ dust systems around early-type stars and for testing the expected correlations with outer disk mass and temperature. It may also allow for the detection of such systems around Sun-like stars. The detailed study of the detected systems with the LBTI (Ertel et al. 2018c) and current and future instruments on the Very Large Telescope Interferometer (Defrère et al. 2018; Ertel et al. 2018a; Kirchschlager et al. 2018) may also allow us to determine the origin of dust in these individual cases and the connection between the HZ dust and hotter dust even closer to the stars, thus helping to understand the origins and dynamics of the various dust species in the HZs of the stars and closer in.

4.2. Potential for the Detailed Study of Specific Targets

In addition to the statistical constraints derived from the HOSTS observations, the data also provide important constraints on specific systems for which exozodiacal dust has been detected or for which strong and interesting upper limits have been found. β UMa and β Leo are examples of relatively strong HZ dust detections in systems with known cold dust. In contrast, α Lyr has a rather low zodi level despite a massive

cold disk, which may be explained by the large size of the outer disk (e.g., given the possible correlation in Figure 5) or the presence of a giant planet preventing dust from migrating inward in the case of the PR drag scenario (Bonsor et al. 2018). ϵ Eri is a nearby, interesting late-type star for exo-Earth imaging, but has a very high HZ dust level which will complicate planet detection. On the other hand, it seems to be the ideal target for studying planet–disk interaction in the HZ. Furthermore, it might be the only Sun-like star in our sample with detected, continuously supplied HZ dust, making it a prototype for studying the relative importance of PR/SW drag and comet delivery around Sun-like stars. The warm dust in the 110 Her system seems to be concentrated relatively far from the star,[21] while the large amount of dust around η Crv is located very close in (Defrère et al. 2015). If a catastrophic event has produced the dust in both systems, this will hint at the separation at which this event occurred. In the PR drag scenario, the dust location around 110 Her could hint at the presence of a massive planet just inside that separation, preventing the dust from migrating farther in (Bonsor et al. 2018). Several systems have high HZ dust levels despite the lack of detected cold dust, which may complicate the target selection for exo-Earth imaging and needs to be understood. Furthermore, in addition to the detected HZ dust, several systems also have hot dust such as α Lyr (Absil et al. 2006) and β Leo (Absil et al. 2013), while others such as ϵ Eri do not. Such systems may allow us to further study the connection between the warm and hot dust and to place additional constraints on the origin of both and the architectures of the planetary systems around those stars.

Our detections can be studied in detail to understand their properties and the diversity of their architectures, and to support our interpretation of the correlations discussed in the previous section between the HZ dust level and other properties of a system. Such studies also improve our understanding of the formation and evolution of the HZ dust and thus increase the ability of models to predict the level of HZ dust in systems that could not be observed by the HOSTS survey. This will critically assist in the target selection for future exo-Earth imaging missions.

We have performed the first such studies on the existing data (Defrère et al. 2015; D. Defrère et al. 2020, in preparation), and the HOSTS science team is currently analyzing the most relevant, remaining detections. Follow-up observations with the LBTI at a wide range of position angles and different wavelengths are critical, however, to derive strong constraints on the architectures of the detected dust disks (Ertel et al. 2018c). Detailed modeling of these data together with available literature data (e.g., Ertel et al. 2011, 2012a; Lebreton et al. 2013; Ertel et al. 2014b; Lebreton et al. 2016) can be used to create a comprehensive picture of each system and to predict its appearance at other wavelengths (e.g., the HZ dust brightness in scattered light). Improving the sensitivity of the LBTI will provide higher quality data for even stronger constraints. Furthermore, the wider community has already taken up the

---

[21] While all our detections are consistent with a moderately increasing excess with aperture size, as expected from a dust distribution analogous to the solar system's zodiacal dust, 110 Her's excess is strongly increasing with photometric aperture size and is the only case with no significant detection in the 8 pix aperture and 13 pix apertures, but a detection in the conservative aperture. Given the large uncertainties, it is however not clear if this is significant, so that this needs to be investigated further by a deeper analysis of the available data and new observations.

first HOSTS publications for further analysis. Bonsor et al. (2018) have developed a model to predict or rule out the presence of giant planets in a system based on the mass and location of an outer belt and the level of HZ dust from our observations. More analyses of our detections will help in calibrating this model to produce accurate constraints.

5. Sample Constraints on Habitable Zone Dust and Implications for Exo-Earth Imaging

The primary objective of the LBTI has been to inform the design of a future exo-Earth imaging space telescope mission. LBTI's mission success criteria describe a desire for "a high confidence prediction of the likely incidence of exozodi dust levels above those considered prohibitive" for such a mission. In this section, we perform a statistical analysis to answer this question, discuss the implications of our results for future exo-Earth imaging and characterization missions, and outline a path for further improvements.

5.1. Sample Constraints on Habitable Zone Dust

In our previous analysis of an early subset of HOSTS observations (Ertel et al. 2018b), we assumed a log-normal distribution of the fraction of stars at a given zodi level (luminosity function) and fitted it to our zodi measurements for different subsamples of stars to determine the median zodi levels of these samples and their uncertainties. We found that (1) a log-normal luminosity function appears inadequate to reproduce the observed distribution of excesses well; instead, a bimodal luminosity function in which most stars have low zodi levels and a few "outliers" have relatively high levels is more likely, and (2) within our statistical uncertainties, there is no significant difference (using Fisher's exact test) between Sun-like stars with and without cold dust as is seen for early-type stars. The former is further supported by our complete survey data, while the latter remains valid. While we see a clear correlation between the detections of cold and HZ dust in our overall sample, the statistics are not good enough to confirm the tentative correlation for Sun-like stars. In particular, the fact that we find LBTI excesses for stars without known debris disks shows that Sun-like stars without far-infrared excesses do not constitute a clean sample of stars with low HZ dust levels. Thus, we do not distinguish between stars with and without detected cold excess for our luminosity function analysis. Because the log-normal distribution is not a good fit to our data and there is reason to believe that a single mechanism inadequately describes the dust production, we use the "free-form" iterative maximum likelihood algorithm described by Mennesson et al. (2014) instead.

For the free-form method, the explored zodi levels for the two spectral-type samples, respectively, are binned and the unknown luminosity function is parameterized through the fraction of stars that have a zodi level in each of the bins. For our analysis, we selected bins of equal width of 1 zodi ranging from 0 zodis to 2000 zodis, an upper boundary consistent with the LBTI measurements of all stars other than η Crv. We excluded the latter star as a clear and extreme outlier to limit the computational effort of our analysis. The fraction of stars in each bin is then adjusted iteratively to maximize the likelihood of observing the data (Mennesson et al. 2014). The median zodi level m was used to characterize the distribution. To determine the uncertainty of the derived distribution, we disturbed this

"nominal" distribution, creating 10^5 new distributions with small deviations from the nominal one. The likelihood of observing the data was computed for each of these distributions, and the profile likelihood theorem was then used to derive 1σ confidence intervals on m from its distribution among them. We derive a median zodi level of $m = 3^{+6}_{-3}$ zodis (95% upper limit: 27 zodis) for Sun-like stars and $m = 2^{+28}_{-2}$ zodis (95% upper limit: 53 zodis) for early-type stars based on the zodi values derived following Section 3.2. The uncertainties on the fraction of stars in each bin of the luminosity function were derived as the range of values encountered for each bin among the distributions that fall within 1σ and 95% probability of the best-fit distribution. The higher upper uncertainties on the median for the early-type stars despite the smaller uncertainties of the individual zodi measurements can be explained by the smaller number of stars and the fact that a larger fraction has significant detections above the best-fit median zodi level.

As an experiment, we recomputed the statistics for our sample of Sun-like stars, but adding the Sun itself with a zodi level defined to be 1 zodi. This did not significantly change our results, which is unsurprising as our results are entirely consistent with 1 star out of 24 Sun-like star having a zodi level of exactly 1 zodi.

Histograms of the best-fit free-form distributions and their 1σ ranges are shown in Figure 7. It is remarkable how similar the distributions are for early-type and Sun-like stars despite the higher detection rate and higher fraction of early-type stars with cold dust compared to Sun-like stars. This further reinforces our earlier conclusion that there is no significant difference in our data between the two spectral-type samples that cannot be explained by the different sensitivity to zodi levels of our observations.

Our results for Sun-like stars are recommended for the yield calculation of future exo-Earth imaging missions and have been adopted by the Habitable Exoplanet Observatory (HabEx; Gaudi et al. 2018) and Large UV-Optical InfraRed Surveyor (LUVOIR; The LUVOIR Team 2018) mission study teams as well as for the Large Interferometer For Exoplanets (LIFE) concept study (Quanz et al. 2018). Histograms of the best-fit free-form distribution and its 1σ range are shown in Figure 7.

5.2. Implications for Exo-Earth Imaging

Direct imaging blends the light of an exoplanet with the light scattered by any surrounding exozodiacal dust. The amount of exozodi contamination is proportional to the sky area of the photometric aperture being used, which in turn depends on the telescope's diffraction-limited beam size. Large telescopes have more compact PSFs and mix less exozodi signal in with the exoplanet signal, while smaller telescopes have larger PSFs that result in more blending of unwanted exozodi signal with planet light. For any given telescope, the exozodi contamination in exoplanet images is worse at longer wavelengths, due to the larger diffraction-limited beam size, and worse for more distant targets where the exoplanet signal is fainter but the exozodi surface brightness is unchanged.

The primary objective of LBTI has been to inform the design of a future exo-Earth imaging space telescope mission. LBTI's mission success criteria describe a desire for "a high confidence prediction of the likely incidence of exozodi dust levels above those considered prohibitive" for such a mission. The science and instrument requirements defined at the 2015 start of the survey were derived from this consideration, given the best
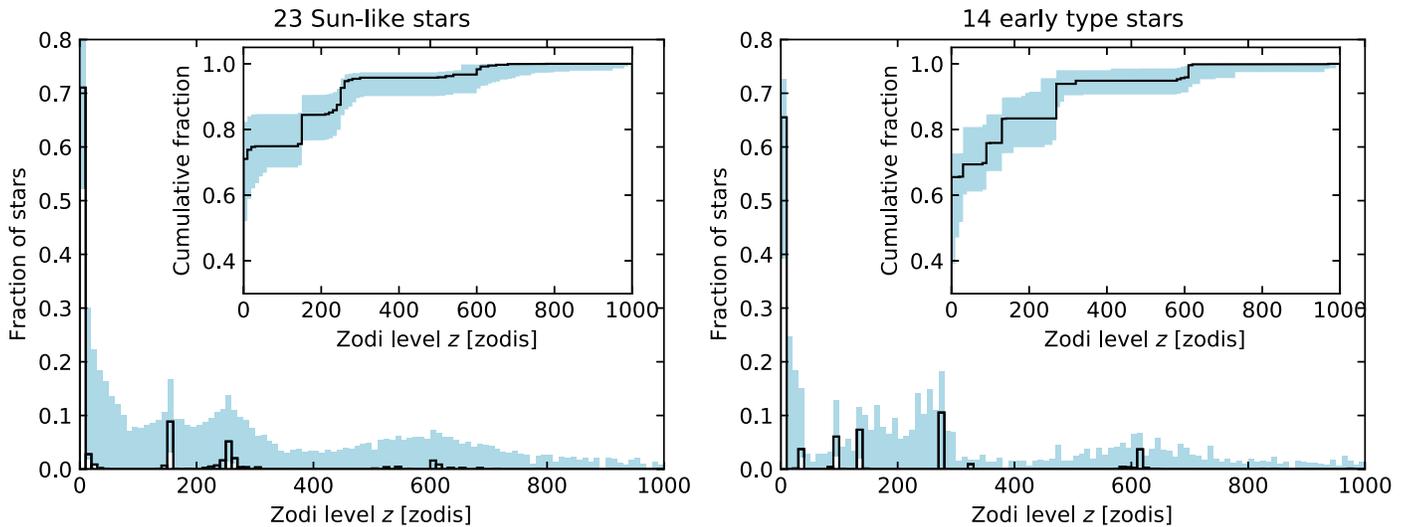
Figure 7. Best-fit free-form luminosity function fit to the HOSTS data for Sun-like stars (left) and early-type stars (right). Both the fraction of stars in each zodi level bin and the cumulative distribution are shown. The black line in each plot shows the best-fit distribution, while the blue bars show the 1σ range for each zodi bin. The original 1 zodi bins used for our analysis are increased to larger bins of 10 zodis for better visualization and reduction of statistical noise in the images.

available knowledge at that time of the impact of exozodiacal dust on such missions. Since then, three mission concept studies have been developed that include exo-Earth direct detection as a major objective: the WFIRST Starshade Rendezvous Probe (Seager et al. 2019), the Habitable Exoplanet Observatory (HabEx; Mennesson & the HabEx STDT team 2019), and the Large UV-Optical InfraRed Surveyor (LUVOIR; Roberge et al. 2019). At the same time, there has been ongoing development of the models that predict the dependence of these missions' science yield on exozodiacal dust levels (Stark et al. 2019).

The survey results in Tables 2 and 3 show that only 25% of stars are dusty enough to be detected with LBTI (median 3σ sensitivity of 69 zodis for early-type stars and 144 zodis for Sun-like stars). At these levels, most stars are not very dusty. The median dust level is inferred from the most likely luminosity function consistent with the HOSTS data set of the Sun-like stars subsample to be 3 zodis. From the distribution of luminosity functions that produce an acceptable fit to the data, the median level may well be below 9 zodis and is likely below 27 zodis which is our 95% upper limit. Furthermore, almost all the HZ exozodi detections occur in systems where cold exo-Kuiper Belt dust has been previously detected by *Spitzer* or *Herschel*; indeed, at 21%, the independently determined frequency of cold dust in nearby stars is comparable (Montesinos et al. 2016) to the incidence of HZ dust at LBTI's sensitivity level. The HOSTS results show that the presence of detectable cold dust is usually a signpost of significant amounts of warm dust in the HZ. The high backgrounds indicated in these systems make them problematic targets for rocky planet spectroscopy, as the integration times needed to characterize atmospheres against these backgrounds are likely to be prohibitive. High zodi levels have also been detected for a number of stars without known cold dust, showing that the correlation is not always reliable. However, the majority of Sun-like stars without cold dust should have zodi levels lower than the values inferred for the full sample, and thus be more favorable targets.

The brightness of our solar system's zodiacal light is our reference point for estimating the exozodiacal backgrounds that

will affect reflected light imaging of HZ rocky planets. It is observed to vary with ecliptic latitude around the sky and also with the ecliptic longitude offset from the Sun (see Table 9.4 of Ryon et al. 2019). We adopt a reference line of sight through our local zodiacal background corresponding to an ecliptic latitude of $30°$ (the median value for targets randomly distributed over the sky) and ecliptic longitude offset of $90°$ (corresponding to an exoplanet target seen at maximum elongation). Along this line of sight, our local zodiacal light has a V-band surface brightness of $V = 22.7$ mag arcsec^{-2} looking outward from Earth. As an external observer's line of sight traverses both inward and outward paths through an optically thin exozodiacal cloud, it is necessary to double the surface brightness relative to the our local observed values. We therefore adopt a correspondence of $V = 22.0$ mag arcsec^{-2} to one zodi of exozodiacal light, scaling this accordingly as we consider the effect of exozodi level on integration times for spectroscopy of HZ rocky planets. At the R band where detections of the the $0.76\,\mu$m O_2 feature will be sought, one zodi of exozodiacal light corresponds to 21.4 mag arcsec^{-2}.

The three exoplanet direct imaging missions currently under consideration would be built around 2.4, 4.0, or 8.0/15.0 m telescope apertures, respectively. Because of their different telescope sizes, each mission could tolerate different amounts of exozodi around a fiducial target star. We first discuss the impact of the best-fit median zodi level from HOSTS, before we discuss the implications of assuming more conservatively zodi levels at our 1σ and 95% upper confidence limits. Following the approach of Roberge et al. (2012),[22] for a solar analog at 10 pc observed in R band ($R = 4.4$) at quadrature, the signal from 3 zodis of dust will exceed that of an Earth analog by factors of 42, 15, 5.4, and 1.4 for the WFIRST Starshade

---

[22] Note that the LBTI nulling measurements were made in the N band and converted to units of zodis using the approach described in Section 3.2 with all its assumptions and limitations. The unit of 1 zodi is a unit of vertical geometrical optical depth (surface density) of dust in a star's HZ. It thus does not depend on the observing wavelength. Predicting the visible-light brightness of the dust based on its zodi level at the relevant observing wavelength is not part of the current paper, we instead use the predictions by Roberge et al. (2012), who give a surface brightness of ≈ 22 mag arcsec^{-2} for a 1 zodi disk viewed at an inclination of $60°$.

Rendezvous, HabEx, LUVOIR 8 m (6.7 m inscribed circle), and LUVOIR 15 m (13.5 m inscribed circle) apertures, respectively. For this target, spectra of the 0.76 μm O_2 feature could be obtained against these backgrounds with continuum S/N $\geqslant$ 10 in reasonable integration times (<60 days) by HabEX and the two LUVOIR apertures at spectral resolution $R = 140$. However, the median exozodi level inferred by our study would not allow the WFIRST Starshade Rendezvous mission to perform $R = 50$ spectroscopy for this target in reasonable integration times.[23]

However, this is not the end of the story. As their apertures increase in size, each mission concept aspires to survey a larger and progressively fainter set of targets. The median brightnesses of their target stars are $V = 3.5, 4.6, 5.4$, and 5.7 for the Starshade Rendezvous, HabEx, LUVOIR 8 m, and LUVOIR 15 m apertures, respectively. The WFIRST Starshade Rendezvous mission is capable of making the above O_2 0.76 μm spectral measurement for its median target with the median exozodi level found by the HOSTS survey, as are all three of the other concepts. This is a key result of the LBTI exozodi efforts: exozodi levels appear to be low enough that all of the current mission concepts for imaging HZ rocky planets could achieve their spectral characterization objectives for their median sample target.

While the median exozodi level found by HOSTS is enabling for future missions, the formal uncertainty in the median remains a cause for concern. The two LUVOIR apertures and the HabEx aperture can still achieve continuum S/N $\geqslant$ 10 for O_2 detection on their median targets with the $+1\sigma$ HOSTS exozodi level of 9 zodis in less than 60 days of integration. For WFIRST's 2.4 m aperture and $R = 50$, this could be achieved only by relaxing the target S/N to $\sim$8. For the upper limit to the median exozodi at 95% confidence (27 zodis), the achievable spectroscopic S/N on the median sample target falls below 10 for the 4.0 m aperture and down to 3 for the 2.4 m aperture, making it doubtful that they could achieve their mission objectives to spectrally characterize the atmospheres of HZ rocky planets. In summary, the remaining uncertainty in exozodi level poses a significant risk to the quality of the spectra that could be obtained with apertures $\leqslant$4 m.

It should be kept in mind that exozodi levels are expected to vary with each individual target. Earth analogs could still be detected and well characterized even with the smaller apertures, if they were present around the nearest stars, or around stars with dust levels below the median of the distribution. When the dust signal is much brighter than the planet, clumps and asymmetries in the dust distribution can become a source of confusion for exoplanet detection. For the 4 m aperture chosen by HabEx, Defrère et al. (2012b) found that this confusion becomes acute above the 20 zodi level, approximately HOSTS' 95% confidence upper limit to the median exozodi for Sun-like stars. Multiepoch imaging could be used to distinguish between the exoplanets and exozodi clumps, as they are expected to have very different phase functions.

5.3. Path for Further Improvements

Currently, the main limitations of the LBTI's nulling interferometric sensitivity are of systematic nature, related to limitations of background and low-frequency detector noise

removal. The current detector of NOMIC is a Raytheon 1024 × 1024 Si:As IBC Aquarius array which is affected by excess low-frequency noise (ELFN, Hoffmann et al. 2014). We are currently evaluating the possibility of upgrading NOMIC with a new H1RG HgCdTe detector with a sensitivity cutoff at a wavelength of 13 μm. This detector promises twice the quantum efficiency of our current detector and not to be affected by ELFN.

In addition, telescope vibrations have been shown to limit our ability to stabilize the optical path delay (OPD) between the two primary apertures. Reducing the power of the strongest vibration (12 Hz, attributed to wind-induced secondary mirror swing arm vibrations) to a level observed during the better half of the HOSTS data acquisition can reduce the statistical uncertainties of our nulling observations by 25% to 50% by improving the null depth of the LBTI. This may be achieved by additional dampening of the vibrations and compensation by more aggressive use of the OPD and Vibration Monitoring System (Böhm et al. 2016). Furthermore, a larger set-point dither pattern (Ertel et al. 2018b) than that used for past HOSTS observations has recently been shown to help achieve a higher accuracy of the NSC by more effectively breaking the degeneracy between imperfect set point and actual astrophysical null signal.

When all these improvements are implemented, the uncertainties of our null measurements will be reduced by a factor of 2 to 3. This will enable us to further improve our constraints on the median zodi level and the exozodi luminosity function around future exo-Earth imaging mission targets through a revived HOSTS survey. Assuming our median zodi level remains unchanged by the new measurements, this will test at a 3σ confidence level whether all mission concepts discussed in Section 5.2 will be able to achieve their spectral characterization goal. If the measured median zodi level changes within our current uncertainties, this could be a deciding factor for which mission should move forward to be able to successfully detect and characterize rocky HZ planets.

In addition, there are open questions about the origin and properties of exozodiacal dust that can be answered by complementary observations at other wavelengths from the visible to mid-infrared range (Gáspár et al. 2019; Mennesson et al. 2019b). Precision interferometric observations in the near- and mid-infrared can provide constraints on the connection between HZ dust and hotter dust closer in which is critical to create a more comprehensive picture of the dust distribution and evolution in the inner regions of planetary systems (Kirchschlager et al. 2017; Ertel et al. 2018a). Scattered-light observations in the visible (Mennesson et al. 2019a) can constrain the dust properties and help make a connection between the dust's infrared thermal emission and its scattered-light brightness, which is critical for future exo-Earth imaging missions. Spectrointerferometry in the LBTI's Fizeau mode (Spalding et al. 2018, 2019) provides another possibility to constrain the dust properties and thus to better predict its brightness at different wavelengths and to learn about its origin and evolution (cometary origin, PR drag, or local production through equilibrium or episodic/catastrophic collisions).

6. Conclusions

The HOSTS survey has been completed successfully after observing 38 stars with a median 3σ sensitivity in the N band of 69 zodis for early-type stars and 144 zodis for Sun-like stars.

---

[23] System spectroscopy throughputs of 0.025, 0.18, 0.09, and 0.08 were adopted for the 2.4 m, 4.0 m, 8.0 m, and 15.0 m apertures, respectively.

In this paper, we have presented and statistically analyzed the final astrophysical null and zodi measurements.

We have detected significant excess around 10 stars and have derived basic detection statistics with respect to other system parameters. Almost all stars with known debris disks also show an excess in our observations with derived HZ dust levels one to three orders of magnitude higher than in our solar system. This correlation suggests an origin of the HZ dust in the outer disk. It seems plausible that the two stars with an outer debris disk but without a HOSTS detection (σ Boo and τ Cet) also have high HZ dust levels but that these are too faint to be detected by our observations with weak upper limits of 140 zodis and 120 zodis, respectively. However, we also found strong detections of HZ dust around stars without a known debris disk which suggests that an alternative scenario for creating this dust may be at play in these systems or that even tenuous cold debris disks that remain undetected by current observations may be a significant source of HZ dust.

After accounting for sensitivity biases in our data, we found no signs of stellar spectral-type or age dependence of the occurrence rates of HZ dust in our data. Although our small number statistics prevent us from detecting small trends, there seems to be no reason to avoid young or early-type stars for exo-Earth imaging missions due to their expected HZ dust content, except insofar as these are more likely to have bright cold debris belts that are an indicator of high HZ dust content. The fact that we detected bright HZ dust disks around gigayear-old stars suggests that these originated either from a recent, stochastic event, or in slowly decaying outer, Kuiper Belt-like debris disks rather than more rapidly decaying asteroid-belt-like disks.

We hypothesized that at least two different types of HZ dust systems may exist: "docile" systems with moderate amounts of dust are likely explained by a continuous delivery of dust to the HZ, while more extreme systems with large amounts of dust are likely better explained by a catastrophic or at least an episodic dust production or delivery mechanism, or a very specific planetary system architecture that may support a high rate of cometary influx. Cometary delivery can contribute to both as a steady flow of comets can be present over a gigayear time span or caused by an episodic event like a late heavy bombardment (Gomes et al. 2005). For Sun-like stars, we may typically be only sensitive enough to detect the latter. Our statistical results can be used to validate future models of the origin and properties of exozodiacal dust. In addition, detailed studies of the detected exozodis will improve our understanding of their architectures and the dust production/delivery mechanisms at play. The combination of an improved understanding of the dust production and delivery in individual systems with population synthesis models calibrated against our detection statistics will improve our predictive power of HZ dust levels for systems that could not be observed.

Fitting a free-form luminosity function to our zodi measurements of Sun-like stars, we derived a median zodi level of $m = 3^{+6}_{-3}$ zodis (95% confidence upper limit: 27 zodis). Our median zodi level would suggest that all currently studied exo-Earth imaging mission concepts will be able to achieve their mission objectives to detect and spectroscopically characterize rocky, HZ planets. However, more precise constraints are still required, in particular for the spectroscopic characterization of the detected planets by missions with a primary aperture $\leqslant 4$ m. We have outlined a path forward to further improve our constraints by moderate instrument upgrades to the LBTI and a revived HOSTS survey.

We find that stars with detected, cold debris disks almost certainly have high HZ dust levels and should be avoided by future exo-Earth imaging missions. We find no indication that young or early-type stars have higher zodi levels than old late-type stars, but our limited sample size prevents us from detecting weak correlations.

The best-fit median HZ dust level derived from our data is only a factor of a few larger than in our solar system and consistent with it within our 1σ uncertainty. This suggests that the solar system's HZ dust content appears typical or only slightly low compared to other, similar stars. However, our uncertainties still permit the typical HZ dust levels around comparable stars to be over an order of magnitude higher than in the solar system.

Despite the successful completion of the HOSTS survey, there are several open questions that need to be answered in the future, specifically with new, more sensitive LBTI observations. The diversity of exozodi systems needs to be better understood by follow-up observations and characterization of the detected systems to better understand the origin of the dust. One caveat of the HOSTS observations is the weak constraints on the dust properties and thus the scattered-light brightness of exozodiacal dust in the visible from the N-band thermal emission observations. Characterizing the detected systems through multiwavelength observations with the LBTI across the N band (and in principle possible down to the K band in case of hotter dust) is critical to better constrain the dust properties and to complement future scattered-light observations of our brightest targets, e.g., with WFIRST. The prospects for follow-up observations of HOSTS detections with the LBTI have been discussed in detail by Ertel et al. (2018c).

Appendix
Modeling Cookbook for LBTI Null Measurements

We provide here a modeling cookbook for LBTI null measurements in the context of exozodiacal dust observations, intended to aid other teams in the modeling of our data using their own tools. A complete description of this modeling approach can be found in Kennedy et al. (2015) with minor updates described by Ertel et al. (2018b).

A.1. High-level Description of the Data

The concept of the data produced by our observations is illustrated in Figure 8. In the case of nulling interferometry, the LBTI combines the light from the two apertures of the LBT in phase opposition in the pupil plane before reimaging the target on the detector. Light at zero OPD between the two sides (on axis or off axis perpendicular to the baseline between the two apertures) is suppressed. An offset on sky with a component in the direction of the interferometric baseline results in a nonzero OPD between the two sides, so that the two light beams are out of phase. This results in a sinusoidal transmission pattern of stripes (Figure 8, second column) perpendicular to the telescope baseline projected on sky with minimum transmission (dark fringes) if the OPD is a multiple of the observing wavelengths and maximum transmission (bright fringes) halfway between the dark fringes. The fringe pattern is always parallel to a great circle through the target and zenith, i.e., the elevation direction due to the LBT's altitude-azimuth mount. This transmission pattern is multiplied (Figure 8, third column) with the angular brightness distribution of the source on sky (Figure 8, first column). The beam combination in the pupil plane and reimaging on the detector mean that the image of the source multiplied by the transmission pattern is then convolved with the single-aperture telescope PSF (Figure 8, fourth column), which produces the final image on the detector. Due to sky rotation during the observations, the sky is rotating under the transmission pattern with parallactic angle. Each of the null measurements in Table 2 is a combination of measurements at a range of parallactic angles.

Because the star is marginally resolved by our observations, part of the starlight is transmitted through the system. Furthermore, there is an instrumental null leak due to imperfections of the system. In practice, these effects are calibrated out during the data reduction, and the null measurements presented in Table 2 are representative of the supposed circumstellar disk alone. The uncertainties from these calibrations are considered in the errors of the null measurements.

A.2. Monochromatic Case

Due to the relatively large uncertainties of our measurements, it is typically sufficient to simplify the problem by considering a monochromatic case. The implications from our broadband observations and the cases where chromatic effects need to be taken into account are discussed in the next section. Here, we provide a step-by-step guide to forward-model a single nulling observation using an arbitrary disk model in the monochromatic case:

1. Simulate a disk image $I(\Delta\alpha, \Delta\delta)$ from the model at 11.11 μm in orientation north up, east left, where $\Delta\alpha$ and $\Delta\delta$ are angular R.A. and decl. sky offsets from the star, respectively.
2. Rotate around the position of the star by the parallactic angle (PA) of the observation[24] to obtain an image $I(\Delta x, \Delta y)$ that is in the correct sky orientation, where $\Delta x = x - x_0$ and $\Delta y = y - y_0$ are Cartesian sky offsets from the Cartesian image coordinates x_0 and y_0 of the star in angular units.
3. Create an image of the transmission pattern $T(\Delta x, \Delta y) = sin^2(\pi \Delta x/p_{\rm null})$, where $p_{\rm null} = \lambda/B$ is the angular period of the transmission pattern at the wavelength $\lambda = 11.11$ μm and (fixed) interferometric baseline $B = 14.4$ m.
4. Create an image of the LBTI's single-aperture PSF. This can be approximated by a 2D Gaussian $G(\Delta x, \Delta y)$ with FWHM = 313 mas (larger than the PSF of an 8.4 m primary aperture due to an undersized pupil stop).
5. A simulated LBTI image is then $J(\Delta x, \Delta y) = [I(\Delta x, \Delta y)T(\Delta x, \Delta y)]\circ G(\Delta x, \Delta y)$, where $\circ$ is the convolution operator.
6. Perform aperture photometry on $J(\Delta x, \Delta y)$ for any of the apertures listed in Table 2. Use a background annulus as it may include some source flux for very extended disks. We chose the inner radius of the background annulus to be the radius of our conservative aperture in Table 2 plus 17.9 mas (one NOMIC pixel), and the outer radius was chosen so that the background annulus has the same area as the photometric aperture.
7. Divide the photometric measurement of the transmitted disk flux by the flux of the star to obtain a simulated null measurement at a given parallactic angle.
8. Average the individual, simulated null measurements and compare the result to the observed null values in Table 2.

A.3. Extension to Broadband Case

The effect of broadband observations is that the transmission pattern is smeared out at large separations ($\gtrsim$300 mas) from the star. This effect is still negligible compared to our measurement uncertainties for smooth dust distributions. Furthermore, observations over a range of parallactic angles also smear the transmission pattern at large separations, which is taken into account by the modeling approach described above. However, for systems with a very large angular size of the HZ (very nearby stars with high luminosity such as α Lyr), if significant disk structures such as azimuthal clumps are considered, or if null measurements over a small parallactic angle range are to be modeled individually, this effect may need to be considered. Strong wavelength dependence of the emission, for example, in the case of a strong spectral silicate feature, may also require considering the broadband effects of our observations.

In this case, the above-described approach needs to be applied to images at a range of wavelengths across the NOMIC N' filter. The transmission of the filter, detector quantum

---

[24] The PA range of our observations can be found in Table 1. At first order, a fixed number of models (e.g., six for one model per nod position) per science pointing (# SCI in Table 1) can be distributed evenly across this PA range. In practice, individual observations are not evenly spaced and have varying sensitivities, and the speed of the sky rotation changes over time. These effects can to some extent be ignored. More in-depth modeling may involve downloading the data from the HOSTS archive at http://lbti.ipac.caltech.edu/ and to simulate observations at the exact PAs of the data as well as weighting the model points by the uncertainties of the individual measurements.
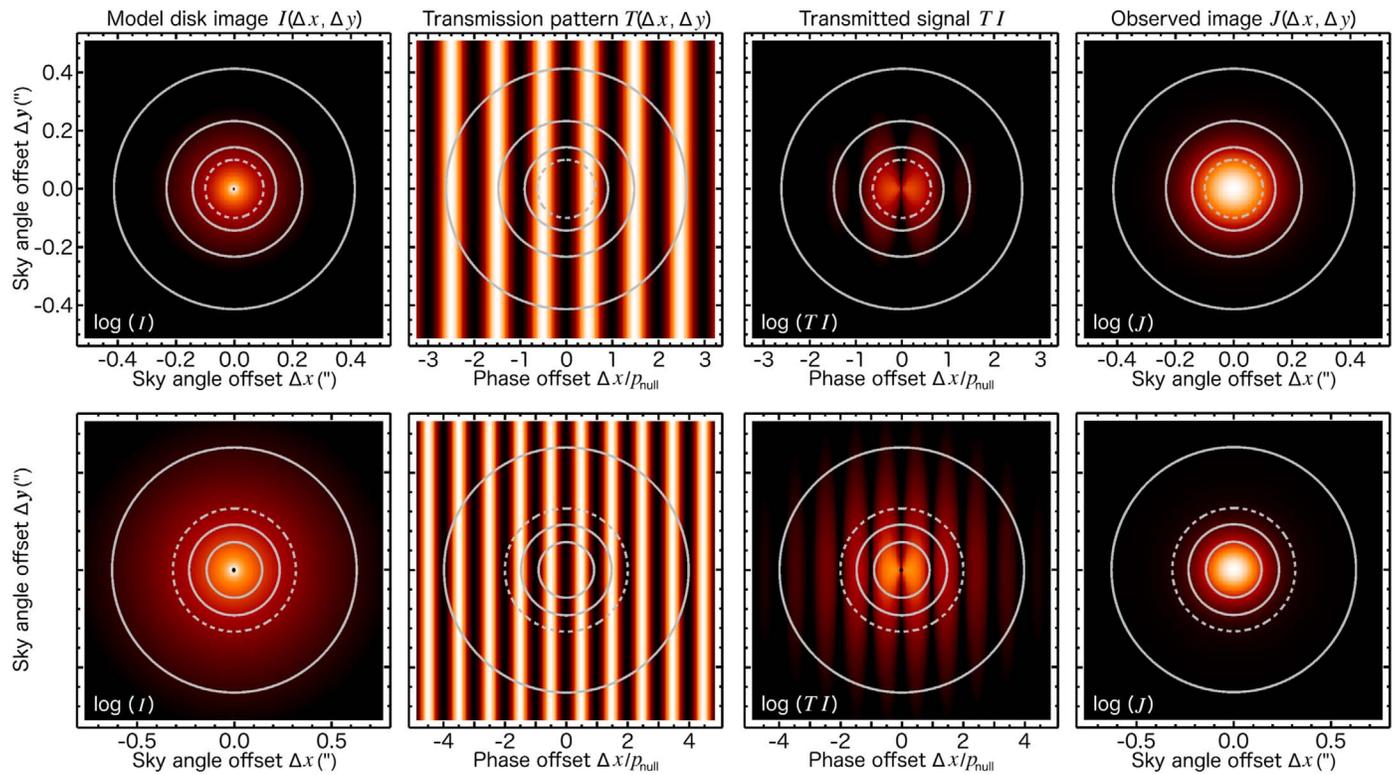
Figure 8. Illustration of the concept of LBTI nulling data and the basic steps of modeling LBTI data. Simulations are shown for stars with luminosities of 1 $L_\odot$ (top) and 10 $L_\odot$ (bottom) at a distance of 10 pc.

efficiency, and the atmospheric transmission in the clear weather in which nulling observations are usually carried out are fairly constant across the filter, with cutoff wavelengths at 9.81 and 12.41 μm. The wavelength dependence of the angular transmission pattern and the single-aperture PSF (scaling linearly with $\lambda/11.11\,\mu$m) need to be taken into account. The simulated null measurements from all wavelengths and parallactic angles can then be averaged and compared to the measurements in Table 2 analogous to point 8 in the previous section.

ORCID iDs

S. Ertel ⓘ https://orcid.org/0000-0002-2314-7289
B. Mennesson ⓘ https://orcid.org/0000-0003-4205-4800
J. Mazoyer ⓘ https://orcid.org/0000-0002-9133-3091
G. Rieke ⓘ https://orcid.org/0000-0003-2303-6519
A. Shannon ⓘ https://orcid.org/0000-0002-0711-4516
K. Stapelfeldt ⓘ https://orcid.org/0000-0002-2805-7338
J. M. Stone ⓘ https://orcid.org/0000-0003-0454-3718
A. J. Weinberger ⓘ https://orcid.org/0000-0001-6654-7859
O. Absil ⓘ https://orcid.org/0000-0002-4006-6237
V. P. Bailey ⓘ https://orcid.org/0000-0002-5407-2806
A. Gaspar ⓘ https://orcid.org/0000-0001-8612-3236
J. M. Leisenring ⓘ https://orcid.org/0000-0002-0834-6140
R. Millan-Gabet ⓘ https://orcid.org/0000-0003-0447-5866
K. M. Morzinski ⓘ https://orcid.org/0000-0002-1384-0063
J.-U. Pott ⓘ https://orcid.org/0000-0003-4291-2078
A. Roberge ⓘ https://orcid.org/0000-0002-2989-3725
A. J. Skemer ⓘ https://orcid.org/0000-0001-6098-3924
K. Y. L. Su ⓘ https://orcid.org/0000-0002-3532-5580
M. C. Wyatt ⓘ https://orcid.org/0000-0001-9064-5598

References

Absil, O., Defrère, D., Coudé du Foresto, V., et al. 2013, A&A, 555, A104
Absil, O., di Folco, E., Mérand, A., et al. 2006, A&A, 452, 237
Astropy Collaboration, Robitaille, T. P., Tollerud, E. J., et al. 2013, A&A, 558, A33
Aumann, H. H. 1985, PASP, 97, 885
Aumann, H. H. 1988, AJ, 96, 1415
Backman, D. E., & Paresce, F. 1993, in Protostars and Planets III, ed. E. H. Levy & J. I. Lunine (Tucson, AZ: Univ. Arizona Press), 1253
Ballering, N. P., Rieke, G. H., & Gáspár, A. 2014, ApJ, 793, 57
Beichman, C. A., Bryden, G., Stapelfeldt, K. R., et al. 2006, ApJ, 652, 1674
Böhm, M., Pott, J.-U., Borelli, J., et al. 2016, Proc. SPIE, 9906, 99062R
Bonsor, A., Augereau, J.-C., & Thébault, P. 2012, A&A, 548, A104
Bonsor, A., Raymond, S. N., & Augereau, J.-C. 2013, MNRAS, 433, 2938
Bonsor, A., Raymond, S. N., Augereau, J.-C., & Ormel, C. W. 2014, MNRAS, 441, 2380
Bonsor, A., Wyatt, M. C., Kral, Q., et al. 2018, MNRAS, 480, 5560
Bordé, P., Coudé du Foresto, V., Chagnon, G., & Perrin, G. 2002, A&A, 393, 183
Bracewell, R. N., & MacPhie, R. H. 1979, Icar, 38, 136
Briesemeister, Z. W., Skemer, A. J., Stone, J. M., et al. 2019, AJ, 157, 244
Chelli, A., Duvert, G., Bourgès, L., et al. 2016, A&A, 589, A112
David, T. J., & Hillenbrand, L. A. 2015, ApJ, 804, 146
Defrère, D., Absil, O., Berger, J. P., et al. 2018, ExA, 46, 475
Defrère, D., Absil, O., den Hartog, R., Hanot, C., & Stark, C. 2010, A&A, 509, A9
Defrère, D., Hinz, P. M., Mennesson, B., et al. 2016, ApJ, 824, 66
Defrère, D., Hinz, P. M., Skemer, A. J., et al. 2015, ApJ, 799, 42
Defrère, D., Lebreton, J., Le Bouquin, J.-B., et al. 2012a, A&A, 546, L9
Defrère, D., Stark, C., Cahoy, K., & Beerer, I. 2012b, Proc. SPIE, 8442, 84420M
Dermott, S. F., Kehoe, T. J. J., Durda, D. D., Grogan, K., & Nesvorný, D. 2002, in Proceedings of Asteroids, Comets, Meteors - ACM 2002, ed. B. Warmbein (Noordwijk: ESA), 319
Dohnanyi, J. S. 1969, JGR, 74, 2531
Eiroa, C., Marshall, J. P., Mora, A., et al. 2013, A&A, 555, A11
Ertel, S., Absil, O., Defrère, D., et al. 2014a, A&A, 570, A128

Ertel, S., Absil, O., Defrère, D., Augereau, J. C., & Mennesson, B. 2018a, ExA, 46, 401
Ertel, S., Defrère, D., Absil, O., et al. 2016, A&A, 595, A44
Ertel, S., Defrère, D., Hinz, P., et al. 2018b, AJ, 155, 194
Ertel, S., Kennedy, G. M., Defrère, D., et al. 2018c, Proc. SPIE, 10698, 106981V
Ertel, S., Marshall, J. P., Augereau, J.-C., et al. 2014b, A&A, 561, A114
Ertel, S., Wolf, S., Marshall, J. P., et al. 2012a, A&A, 541, A148
Ertel, S., Wolf, S., Metchev, S., et al. 2011, A&A, 533, A132+
Ertel, S., Wolf, S., & Rodmann, J. 2012b, A&A, 544, A61
Faramaz, V., Ertel, S., Booth, M., Cuadra, J., & Simmonds, C. 2017, MNRAS, 465, 2352
Gáspár, A., Apai, D., Augereau, J.-C., et al. 2019, BAAS, 51, 69
Gáspár, A., & Rieke, G. H. 2014, ApJ, 784, 33
Gáspár, A., Rieke, G. H., & Balog, Z. 2013, ApJ, 768, 25
Gaudi, B. S., Seager, S., Mennesson, B., et al. 2018, arXiv:1809.09674
Gezari, D. Y., Schmitz, M., Pitts, P. S., & Mead, J. M. 1993, Far Infrared Supplement: Catalog of Infrared Observations (3rd ed.; Greenbelt, MD: NASA)
Gomes, R., Levison, H. F., Tsiganis, K., & Morbidelli, A. 2005, Natur, 435, 466
Greaves, J. S., Wyatt, M. C., Holland, W. S., & Dent, W. R. F. 2004, MNRAS, 351, L54
Hanot, C., Mennesson, B., Martin, S., et al. 2011, ApJ, 729, 110
Hinz, P. M., Angel, J. R. P., Hoffmann, W. F., et al. 1998, Natur, 395, 251
Hinz, P. M., Angel, J. R. P., Woolf, N. J., Hoffmann, W. F., & McCarthy, D. W. 2000, Proc. SPIE, 4006, 349
Hinz, P. M., Defrère, D., Skemer, A., et al. 2016, Proc. SPIE, 9907, 990704
Hoffmann, W. F., Hinz, P. M., Defrère, D., et al. 2014, Proc. SPIE, 9147, 91471O
Hunter, J. D. 2007, CSE, 9, 90
Kelsall, T., Weiland, J. L., Franz, B. A., et al. 1998, ApJ, 508, 44
Kennedy, G. M., & Piette, A. 2015, MNRAS, 449, 2304
Kennedy, G. M., & Wyatt, M. C. 2013, MNRAS, 433, 2334
Kennedy, G. M., & Wyatt, M. C. 2014, MNRAS, 444, 3164
Kennedy, G. M., Wyatt, M. C., Bailey, V., et al. 2015, ApJS, 216, 23
Kharchenko, N. V., Scholz, R., Piskunov, A. E., Roeser, S., & Schilbach, E. 2007, yCat, 3254, 0
Kimura, H., Kunitomo, M., Suzuki, T. K., et al. 2020, P&SS, 183, 104581
Kirchschlager, F., Wolf, S., Brunngräber, R., et al. 2018, MNRAS, 473, 2633
Kirchschlager, F., Wolf, S., Krivov, A. e. V., Mutschke, H., & Brunngräber, R. 2017, MNRAS, 467, 1614
Koerner, D. W., Kim, S., Trilling, D. E., et al. 2010, ApJL, 710, L26
Kral, Q., Krivov, A. V., Defrère, D., et al. 2017, AstRv, 13, 69
Kral, Q., Wyatt, M. C., Triaud, A. H. M. J., et al. 2018, MNRAS, 479, 2649
Lawler, S. M., Beichman, C. A., Bryden, G., et al. 2009, ApJ, 705, 89
Lebreton, J., Beichman, C., Bryden, G., et al. 2016, ApJ, 817, 165
Lebreton, J., van Lieshout, R., Augereau, J.-C., et al. 2013, A&A, 555, A146
Lisse, C. M., Wyatt, M. C., Chen, C. H., et al. 2012, ApJ, 747, 93
Mannings, V., & Barlow, M. J. 1998, ApJ, 497, 330
Marino, S., Bonsor, A., Wyatt, M. C., & Kral, Q. 2018, MNRAS, 479, 1651
Marino, S., Wyatt, M. C., Panić, O., et al. 2017, MNRAS, 465, 2595
Marshall, J. P., Cotton, D. V., Bott, K., et al. 2016, ApJ, 825, 124
Marshall, J. P., Krivov, A. V., del Burgo, C., et al. 2013, A&A, 557, A58
Mawet, D., Hirsch, L., Lee, E. J., et al. 2019, AJ, 157, 33
Meng, H. Y. A., Su, K. Y. L., Rieke, G. H., et al. 2014, Sci, 345, 1032

Mennesson, B., Bailey, V., Kasdin, J., et al. 2019a, arXiv:1909.02161
Mennesson, B., Defrère, D., Nowak, M., et al. 2016, Proc. SPIE, 9907, 99070X
Mennesson, B., Kennedy, G., Ertel, S., et al. 2019b, BAAS, 51, 324
Mennesson, B., Millan-Gabet, R., Serabyn, E., et al. 2014, ApJ, 797, 119
Mennesson, B., Serabyn, E., Hanot, C., et al. 2011, ApJ, 736, 14
Mennesson, B. & the HabEx STDT team 2019, Habitable Exoplanet Observatory (HabEx), https://www.jpl.nasa.gov/habex/
Mérand, A., Bordé, P., & Coudé du Foresto, V. 2005, A&A, 433, 1155
Metcalfe, T. S., Creevey, O. L., & Davies, G. R. 2015, ApJL, 811, L37
Millan-Gabet, R., Serabyn, E., Mennesson, B., et al. 2011, ApJ, 734, 67
Montesinos, B., Eiroa, C., Krivov, A. V., et al. 2016, A&A, 593, A51
Morales, F. Y., Rieke, G. H., Werner, M. W., et al. 2011, ApJL, 730, L29
Moro-Martín, A., & Malhotra, R. 2003, AJ, 125, 2255
Nesvorný, D., Jenniskens, P., Levison, H. F., et al. 2010, ApJ, 713, 816
Nuñez, P. D., Scott, N. J., Mennesson, B., et al. 2017, A&A, 608, A113
Ochsenbein, F., Bauer, P., & Marcout, J. 2000, A&AS, 143, 23
Poppe, A. R., Lisse, C. M., Piquette, M., et al. 2019, ApJL, 881, L12
Quanz, S. P., Kammerer, J., Defrère, D., et al. 2018, Proc. SPIE, 10701, 107011I
Reidemeister, M., Krivov, A. V., Stark, C. C., et al. 2011, A&A, 527, A57
Rieke, G. H., Gáspár, A., & Ballering, N. P. 2016, ApJ, 816, 50
Rieke, G. H., Su, K. Y. L., Stansberry, J. A., et al. 2005, ApJ, 620, 1010
Roberge, A., Chen, C. H., Millan-Gabet, R., et al. 2012, PASP, 124, 799
Roberge, A., Petersen, B., Fisher, D. & the LUVOIR STDT team 2019, LUVOIR Study, http://asd.gsfc.nasa.gov/luvoir/
Ryon, J. et al. (ed.) 2019, Advanced Camera for Surveys Instrument Handbook for Cycle 28 (Baltimore, MD: STScI), https://hst-docs.stsci.edu/display/ACSIHB/
Seager, S., Kasdin, J., Booth, J., et al. 2019, Starshade Rendezvous Probe, NASA Tech. Rep., GSFC-E-DAA-TN70889, https://ntrs.nasa.gov/archive/nasa/casi.ntrs.nasa.gov/20190028272.pdf
Sezestre, É., Augereau, J. C., & Thébault, P. 2019, A&A, 626, A2
Shannon, A., Mustill, A. J., & Wyatt, M. 2015, MNRAS, 448, 684
Sierchio, J. M., Rieke, G. H., Su, K. Y. L., & Gáspár, A. 2014, ApJ, 785, 33
Spalding, E., Hinz, P., Ertel, S., Maier, E., & Stone, J. 2018, Proc. SPIE, 10701, 107010J
Spalding, E., Hinz, P., Morzinski, K., et al. 2019, arXiv:1908.11023
Stark, C. C., Belikov, R., Bolcar, M. R., et al. 2019, JATIS, 5, 024009
Stark, C. C., & Kuchner, M. J. 2008, ApJ, 686, 637
Stark, C. C., Roberge, A., Mandell, A., et al. 2015, ApJ, 808, 149
Stark, C. C., Shaklan, S., Lisman, D., et al. 2016, JATIS, 2, 041204
Stock, N. D., Su, K. Y. L., Liu, W., et al. 2010, ApJ, 724, 1238
Stone, J. M., Skemer, A. J., Hinz, P., et al. 2018a, Proc. SPIE, 10702, 107023F
Stone, J. M., Skemer, A. J., Hinz, P. M., et al. 2018b, AJ, 156, 286
Su, K. Y. L., Jackson, A. P., Gáspár, A., et al. 2019, AJ, 157, 202
Su, K. Y. L., Rieke, G. H., Stansberry, J. A., et al. 2006, ApJ, 653, 675
The LUVOIR Team 2018, arXiv:1809.09668
Thureau, N. D., Greaves, J. S., Matthews, B. C., et al. 2014, MNRAS, 445, 2558
Trilling, D. E., Bryden, G., Beichman, C. A., et al. 2008, ApJ, 674, 1086
van Leeuwen, F. 2007, A&A, 474, 653
Weinberger, A. J., Bryden, G., Kennedy, G. M., et al. 2015, ApJS, 216, 24
Wenger, M., Ochsenbein, F., Egret, D., et al. 2000, A&AS, 143, 9
Wyatt, M. C. 2005, A&A, 433, 1007
Zuckerman, B. 2019, ApJ, 870, 27